RESEARCH ARTICLE

Key Points:
- Peroxide scavenging efficiencies derived from measurements
- Hydrogen peroxide is readily removed by storms
- Methyl hydrogen peroxide scavenging correlated with cloud physics and entrainment rate

Correspondence to:
M. C. Barth,
barthm@ucar.edu

Convective transport and scavenging of peroxides by thunderstorms observed over the central U.S. during DC3

M. C. Barth[1], M. M. Bela[2,3], A. Fried[4], P. O. Wennberg[5], J. D. Crounse[5], J. M. St. Clair[6], N. J. Blake[7], D. R. Blake[7], C. R. Homeyer[8], W. H. Brune[9], L. Zhang[9], J. Mao[10,11], X. Ren[12], T. B. Ryerson[13], I. B. Pollack[14], J. Peischl[13,15], R. C. Cohen[16], B. A. Nault[16,17], L. G. Huey[18], X. Liu[18], and C. A. Cantrell[2]

[1]Atmospheric Chemistry Observations and Modeling Laboratory and Mesoscale and Microscale Meteorology Laboratory, National Center for Atmospheric Research, Boulder, Colorado, USA, [2]Department of Atmospheric and Oceanic Sciences, University of Colorado Boulder, Boulder, Colorado, USA, [3]Laboratory for Atmospheric and Space Physics, University of Colorado Boulder, Boulder, Colorado, USA, [4]Institute for Arctic and Alpine Research, University of Colorado Boulder, Boulder, CO, USA, [5]Division of Geology and Planetary Sciences, California Institute of Technology, Pasadena, California, USA, [6]Joint Center for Earth Systems Technology, University of Maryland, Baltimore County/NASA Goddard Space Flight Center, Greenbelt, Maryland, USA, [7]Department of Chemistry, University of California, Irvine, California, USA, [8]School of Meteorology, University of Oklahoma, Norman, Oklahoma, USA, [9]Department of Meteorology, Pennsylvania State University, University Park, Pennsylvania, USA, [10]Program in Atmospheric and Oceanic Sciences, Princeton University, Princeton, New Jersey, USA, [11]Geophysical Fluid Dynamics Laboratory, NOAA, Princeton, New Jersey, USA, [12]NOAA-Air Resources Laboratory, College Park, Maryland, USA, [13]Chemical Sciences Division, Earth System Research Laboratory, National Oceanic and Atmospheric Administration, Boulder, Colorado, USA, [14]Atmospheric Sciences Department, Colorado State University, Fort Collins, Colorado, USA, [15]Cooperative Institute for Research in Environmental Sciences, University of Colorado Boulder, Boulder, Colorado, USA, [16]University of California, Berkeley, California, USA, [17]Now at Department of Chemistry and Biochemistry and Cooperative Institute for Research in Environmental Sciences, University of Colorado Boulder, Boulder, Colorado, USA, [18]Georgia Institute of Technology, Atlanta, Georgia, USA

Abstract One of the objectives of the Deep Convective Clouds and Chemistry (DC3) field experiment was to determine the scavenging of soluble trace gases by thunderstorms. We present an analysis of scavenging of hydrogen peroxide (H_2O_2) and methyl hydrogen peroxide (CH_3OOH) from six DC3 cases that occurred in Oklahoma and northeast Colorado. Estimates of H_2O_2 scavenging efficiencies are comparable to previous studies ranging from 79 to 97% with relative uncertainties of 5–25%. CH_3OOH scavenging efficiencies ranged from 12 to 84% with relative uncertainties of 18–558%. The wide range of CH_3OOH scavenging efficiencies is surprising, as previous studies suggested that CH_3OOH scavenging efficiencies would be <10%. Cloud chemistry model simulations of one DC3 storm produced CH_3OOH scavenging efficiencies of 26–61% depending on the ice retention factor of CH_3OOH during cloud drop freezing, suggesting ice physics impacts CH_3OOH scavenging. The highest CH_3OOH scavenging efficiencies occurred in two severe thunderstorms, but there is no obvious correlation between the CH_3OOH scavenging efficiency and the storm thermodynamic environment. We found a moderate correlation between the estimated entrainment rates and CH_3OOH scavenging efficiencies. Changes in gas-phase chemistry due to lightning production of nitric oxide and aqueous-phase chemistry have little effect on CH_3OOH scavenging efficiencies. To determine why CH_3OOH can be substantially removed from storms, future studies should examine effects of entrainment rate, retention of CH_3OOH in frozen cloud particles during drop freezing, and lightning-NO_x production.

1. Introduction

To understand the radiative impact of ozone in the upper troposphere (UT), ozone chemical sources in the UT must be quantified. Ozone (O_3) is produced by the reactions between peroxy radicals (e.g., hydroperoxy and methylperoxy radicals, HO_2 and CH_3OO, respectively) and nitric oxide (NO) to form nitrogen dioxide (NO_2), which subsequently photodissociates to form O_3. Thus, odd hydrogen ($HO_x = OH + HO_2$; OH is hydroxyl radical) and nitrogen oxides ($NO_x = NO + NO_2$) are key precursors to O_3. Although the primary formation of HO_x radicals is from O_3 photodissociation, oxidation of volatile organic compounds (VOCs), as well as their photodissociation, is also important. A source of these VOCs and NO_x in the UT is in convective outflow regions, where VOCs are transported from the boundary layer (BL) to the UT and NO_x is formed from lightning.

However, many key HO_x precursors, including formaldehyde (CH_2O), hydrogen peroxide (H_2O_2), and methyl hydrogen peroxide (CH_3OOH), are soluble and can be partially removed from the atmosphere via dissolution into cloud drops that grow into rain, snow, graupel, and hail precipitating to the ground. Quantifying the fraction of HO_x precursors that are scavenged (or conversely transported to the UT) improves the estimation of O_3 production in convective outflow regions. In this paper, we determine the scavenging efficiencies (SE) of H_2O_2 and CH_3OOH based on aircraft measurements obtained during the Deep Convective Cloud and Chemistry (DC3) field experiment [*Barth et al.*, 2015]. A. Fried et al. (Convective transport of formaldehyde to the upper troposphere and lower stratosphere and associated scavenging in thunderstorms over the central United States during the 2012 DC3 study, submitted to *Journal of Geophysical Research*, 2016) perform a similar analysis for CH_2O, while *Bela et al.* [2016] evaluate the convective transport of nitric acid, H_2O_2, CH_2O, sulfur dioxide, and CH_3OOH in a three-dimensional cloud chemistry model with observations and calculate the fraction of these species removed for four DC3 thunderstorm cases.

Previous studies suggest convective transport of HO_x precursors play an important role in controlling O_3 mixing ratios in the UT. Measurements of UT HO_x during the NASA Stratospheric Tracers of Atmospheric Transport (STRAT) (1996) campaign occasionally exceeded theoretical estimates of HO_x concentrations, suggesting an additional source of UT HO_x that was proposed to be convective transport of CH_2O, H_2O_2, and CH_3OOH [*Jaeglé et al.*, 1997; *Prather and Jacob*, 1997; *Wennberg et al.*, 1998]. Measurements from the NASA Pacific Exploratory Mission (PEM)-Tropics (1999) campaign revealed an enhancement of CH_3OOH and a lack of enhancement of H_2O_2 in aged convective outflow over the tropical Pacific, supporting the importance of convective transport for sources of hydrogen oxide radicals in the upper troposphere [*Ravetta et al.*, 2001]. *Cohan et al.* [1999] estimated that H_2O_2 had 55–70% scavenging efficiency based on measurements of tropical oceanic convection, while CH_3OOH showed no apparent scavenging. Peroxide measurements from the NASA Intercontinental Chemical Transport Experiment (INTEX-NA) field campaign revealed that H_2O_2 was depleted, while CH_3OOH was enhanced in convective outflow regions compared to the background UT [*Snow et al.*, 2007]. These prior measurements in STRAT, PEM Tropics-B, and INTEX-A did not gather simultaneous inflow and outflow trace gas measurements of convection to allow for estimates of peroxide scavenging. An intercomparison study of cloud-scale chemistry models [*Barth et al.*, 2007b] showed a large variation in predictions of CH_2O and H_2O_2 that depended on whether or not the trace gas was retained in frozen particles (snow, graupel, or hail).

Other previous studies have indicated an unexpected reduced amount of CH_3OOH in the marine boundary layer impacted by clouds compared to the reduction that would be expected due to gas-phase photochemistry. *Fried et al.* [2003] discuss conditions at very low NO mixing ratios (<5 parts per trillion by volume (pptv)) where box model calculations predicted CH_3OOH mixing ratios to be 2–3 times greater than nearby CH_3OOH observations. While we expect CH_3OOH to be higher at low NO mixing ratios than at high NO, the theoretical estimates are much greater than observed, suggesting that additional losses reduce CH_3OOH in reality. In the DC3 environment, NO mixing ratios were rarely (if at all) this low. However, the reverse situation could exist where increases in NO mixing ratios from lightning production enable peroxy radicals to react with NO instead of with each other, thereby preventing the formation of peroxides.

Although H_2O_2 is highly soluble, its partitioning between gas and aqueous phases, as well as that for CH_3OOH, should be in Henry's law equilibrium based on theoretical calculations and analysis of field measurements [*Barth et al.*, 1989; *MacDonald et al.*, 1995]. Because the Henry's law equilibrium coefficients for H_2O_2 are over 2 orders of magnitude higher than those of CH_3OOH, we expect that more H_2O_2 than CH_3OOH will be removed by cloud and precipitation than CH_3OOH. However, we will show that CH_3OOH is sometimes removed more than expected, even as much as H_2O_2.

In this paper we examine the behavior of CH_3OOH and H_2O_2 observed during DC3. The scavenging efficiencies of H_2O_2 and CH_3OOH are derived from measurements of these peroxides and tracers of transport that were collected during the DC3 field experiment. The DC3 campaign and the instrument techniques used in the analysis are described in the next section. We then present the analysis method for determining each storm's entrainment rate and the peroxide scavenging efficiencies. We also use cloud-resolved three-dimensional and box model simulations to investigate physical and chemical processes affecting the peroxide scavenging. Results for six DC3 storm cases are presented. In addition to discussing the uncertainties of

Table 1. List of Data and Instruments Used in the Analysis

Species/Parameter	Instrument[a]	Uncertainty
H_2O_2, CH_3OOH	CIT-CIMS	H_2O_2 (pptv): $75 + 0.5$ [H_2O_2] CH_3OOH (pptv): $30 + 0.4$[CH_3OOH] at H_2O vapor < 230 ppmv $30 + (-9.1 + \log_{10}[H_2O])$ [CH_3OOH] at H_2O vapor > 230 ppmv
n-butane, i-butane, n-pentane, i-pentane	WAS	5% or 3 pptv
NO, NO_2[b]	CSD CL	NO (pptv): $10 + 0.04$ [NO] NO_2 (pptv): $20 + 0.06$ [NO_2]
NO_2, MPN[c]	TD-LIF	NO_2: 5% MPN: 40%
OH, HO_2	ATHOS	32%
SO_2	GT-CIMS	15%
H_2O vapor	DLH	5% or 1 ppmv
Pressure, temperature, 3-D winds	MMS	Pressure: 0.5% Temperature: 0.2% Winds: 3%
Ice water content	2DS	Not available

[a]CIT-CIMS is California Institute of Technology chemical ionization mass spectrometry; WAS is the Whole Air Sampler that uses gas chromatography; CSD CL is NOAA Chemical Science Division chemiluminescence; TD-LIF is thermal dissociation—laser-induced fluorescence; ATHOS is Airborne Tropospheric Hydrogen Oxides Sensor that uses laser-induced fluorescence; GT-CIMS is Georgia Institute of Technology chemical ionization mass spectrometry; DLH is diode laser hygrometer that uses differential absorption spectroscopy; MMS is Meteorological Measurement System; 2DS is two-dimensional stereo probe.
[b]The NO_2 measurement should be interpreted as the sum of NO_2 and MPN based on the findings of *Browne et al.* [2011].
[c]MPN is methyl peroxy nitrate.

the calculations, we show how the peroxide scavenging efficiencies vary with some key storm parameters, including the storm physics and chemistry.

2. Methods

2.1. Observations

The DC3 field experiment took place in May and June 2012, sampling thunderstorms in northeast Colorado, west Texas to central Oklahoma, and northern Alabama. Ground-based facilities documented the storm kinematics, physical structure, and lightning location. Three aircraft, the NASA DC-8, the NSF/NCAR Gulfstream V (GV), and the DLR Falcon 20, sampled the inflow and outflow regions of the storms to quantify the composition of these regions. *Barth et al.* [2015] present further details on the DC3 field experiment. Both the DC-8 and GV aircraft collected peroxide measurements. However, wingtip-to-wingtip intercomparisons showed that the peroxide measurements from the two instruments did not always agree. Because these differences were not constantly systematic, this paper uses measurements solely from the DC-8 aircraft since it flew in both inflow and outflow regions for each case analyzed (whereas the GV flew most often in outflow regions).

The DC-8 aircraft was extensively instrumented with trace gas and aerosol instruments [*Barth et al.*, 2015]. A list of the data and instruments used in this study is given in Table 1. Horizontal winds, temperature, and pressure measurements on the DC-8 were obtained via the meteorological measurement system (MMS). Ice water content (IWC) was measured aboard the DC-8 aircraft by the SPEC two-dimensional Stereo (2DS) probe [*Lawson et al.*, 2006].

On the DC-8 aircraft, H_2O_2 and CH_3OOH were measured using time-of-flight (ToF-CIMS) mass filter and tandem quadrupole mass filter (T-CIMS) chemical ionization mass spectrometers (CIMS), respectively. The rapid-scan collection of the ToF-CIMS instrument provides high temporal resolution (1 Hz or faster) and simultaneous data products for all masses [*Nguyen et al.*, 2015]. The ToF-CIMS instrument was built by upgrading the mass analyzer of the single quadrupole CIT-CIMS instrument [*Crounse et al.*, 2006]. The T-CIMS provides parent-daughter mass analysis, enabling measurement of compounds precluded from quantification by a single mass analyzer CIMS due to mass interferences (e.g., CH_3OOH) or the presence of isobaric compounds

(e.g., isoprene oxidation products) [*Paulot et al.*, 2009; *St. Clair et al.*, 2010]. Instrument operation details, including gas sampling, calibration, and zeroing, were retained from the previous instrument and are described in *Crounse et al.* [2006] for H_2O_2 and *St. Clair et al.* [2010] for CH_3OOH. Calibrations for H_2O_2 and CH_3OOH are performed once per hour during flight using calibration standards for H_2O_2 (evolved from urea-hydrogen peroxide) and CH_3OOH (from a diffusion vial). Note that the uncertainties for H_2O_2 (>50%) and CH_3OOH (~80% at low altitude and ~40% at high altitude) are high and contribute the largest uncertainty to the analysis performed in this study. The water dependence of the CH_3OOH measurement sensitivities are discussed by *St. Clair et al.* [2010], who include an expression for the estimated water dependence of the CH_3OOH measurement uncertainty, which is applied in this study (Table 1).

The nonmethane hydrocarbons *n*-butane, *i*-butane, *n*-pentane, and *i*-pentane are used to estimate the entrainment rate for each storm. On the DC-8, these hydrocarbons were measured using the whole air sampler (WAS), which pumps a sample of air into a previously evacuated canister with an approximately 1 min fill time (up to 2 min at high altitude) that is analyzed in the laboratory by gas chromatography [*Colman et al.*, 2001; *Simpson et al.,* 2010]. The sampling frequency was typically every 2 to 5 min but increased when inflow and outflow regions were sampled. Assuming a 200 m s^{-1} aircraft speed, the horizontal coverage for 60, 90, and 120 s fill times equates to 12, 18, and 24 km, respectively. With this horizontal resolution, the canister samples adequately captured the inflow and outflow regions of the storms. The sampling of the inflow and outflow regions was done during level flight legs giving a vertical resolution in these regions of 0.1 km or less. The vertical resolution during aircraft profiles depends on the rate of climb and altitude. During vertical profiles, the fill time typically occurred over a 0.4–0.5 km vertical distance, and between canister samples the vertical distance was 0.4–0.6 km.

Aircraft measurements of OH, HO_2, sulfur dioxide (SO_2), NO, NO_2, and methyl peroxy nitrate (MPN) are used in assessing whether CH_3OOH scavenging efficiencies are correlated with these trace gases or to examine the gas-phase CH_3OOH production. The HO_x radicals, OH and HO_2, were measured by the Pennsylvania State University Airborne Tropospheric Hydrogen Oxides Sensor (ATHOS), which is a laser-induced fluorescence technique [*Faloona et al.*, 2004]. SO_2 is measured with the Georgia Institute of Technology CIMS [*Kim et al.*, 2007]. NO was measured by ozone-induced chemiluminescence, O_3 was measured by NO-induced chemiluminescence, and NO_2 was photolyzed to NO using ultraviolet photolysis prior to ozone chemiluminescence detection [*Pollack et al.*, 2011]. The NO_2 data before 11 June 2012 are from the University of California-Berkeley thermal dissociation-laser-induced fluorescence (TD-LIF) instrument [*Thornton et al.*, 2000; *Nault et al.*, 2015]. MPN mixing ratios were also measured with the TD-LIF instrument as described by *Nault et al.* [2015]. Carbon monoxide (CO), used to identify biomass burning plumes and stratospheric air, was measured with a differential absorption mid-IR diode laser spectrometer [*Sachse et al.*, 1991].

Next Generation Weather Radar (NEXRAD) program Weather Surveillance Radar, 1988 Doppler data [*Crum and Alberty*, 1993] are used to understand the storm structure and to estimate the distance of the DC-8 aircraft sampling the outflow from the nearest storm core. Data from multiple radars, which are S band (10 cm wavelength) radars, are processed to produce three-dimensional composites following the procedure described in *Homeyer* [2014] and updated in *Homeyer and Kumjian* [2015]. Radiosonde data from soundings launched in the prestorm environment are used to determine the thermodynamic environment of the storm. Radiosondes in Colorado are from the NCAR Mobile Integrated Sounding System and those in Oklahoma from the National Severe Storms Laboratory (NSSL). The National Weather Service North Platte sounding was used for the 18 May storm observed in southwest Nebraska. The convective available potential energy (CAPE), 0–6 km vertical wind shear, depth from cloud base to the freezing level, and depth from the freezing level to the −40°C isotherm were calculated from the soundings. The CAPE is determined using mixed layer mean temperature, where the mixed layer is defined between the surface and 100 hPa above the surface.

Six case studies were chosen from the DC3 data set (Table 2) based on the availability of DC-8 inflow and outflow data and getting a variety of convection types. Four of these cases were in the northeast Colorado and southwest Nebraska region, and two were in Oklahoma. The cases are primarily severe convection, with CAPE ranging from 900 to 3100 J kg^{-1} and 0–6 km vertical wind shear range of 12–24 m s^{-1}. The depth of the cloud where $T > 0°C$ (where only liquid water cloud physics occurs) varies substantially among storms. The Colorado convective storms have much shallower depths between cloud base and the freezing level than Oklahoma convection, but this depth increases from mid-May to late June. The depth from the freezing level

Table 2. DC3 Cases Investigated

Date	Location	CAPE (J kg^{-1})	0–6 km Vertical Wind Shear (m s^{-1})	Cloud base to Freezing Level Depth (m)	Freezing Level to −40°C Depth (m)
18 May 2012	Southwest Nebraska	1144	12.1	121	4910
29 May 2012	Northern Oklahoma	3113	19.0	2505	5780
02 June 2012	Northeast Colorado	918	13.2	640	5172
06 June 2012	Northeast Colorado	2981	17.5	1157	5145
16 June 2012	Central Oklahoma	3049	15.9	2762	5803
22 June 2012	Southwest Nebraska	2563	24.2	1750	5229

to $T = -40$°C, the temperature where cloud drops homogeneously freeze, is fairly consistent among storms with depths from 4900 to 5200 m for Colorado storms and ~5800 m for Oklahoma storms.

2.2. Analysis Method

Calculations of scavenging efficiencies from aircraft observations have been done previously by using a multicomponent mixture model. *Cohan et al.* [1999] considered two components, one being the inflow region and the second being the upper troposphere where the convective outflow resides. *Borbon et al.* [2012] used three components (BL, free troposphere, and UT), and *Yang et al.* [2015] used four components (BL, buffer layer, clean layer, and UT, where the buffer layer extends from the BL to 7 km altitude and the clean air layer extends from 7 km to 9.5 km where the UT layer begins), adding entrainment of free troposphere air. *Luo et al.* [2010] estimated entrainment in every 1 km layer of the deep convection. Here and as done by A. Fried et al. (submitted manuscript, 2016), we combine the methods of these previous studies to determine the scavenging efficiencies of trace gases.

Measurements from the inflow and outflow regions of the storm, as well as the free troposphere, were used to compute the scavenging efficiencies. The DC-8 aircraft obtained these measurements by first sampling the inflow BL composition at several altitudes, including a flight leg above the BL top, and then spiraling up to the anvil outflow region where several across-anvil passes were made (Figure 1). The anvil passes were typically several kilometers downwind of the storm core tops in order to keep the aircraft a safe distance from damaging hail and turbulence. Thus, some degree of anvil dilution and chemistry is imparted on the trace gas mixing ratios before the DC-8 aircraft collects the measurements. To minimize the impact of dilution and chemistry, we use outflow data that are closest to the storm core tops. In section 4, we show that there is no correlation between the scavenging efficiencies and the estimated time for the air parcels to reach the aircraft from the storm core tops. A. Fried et al. (submitted manuscript, 2016) employed a similar data analysis but instead used 1 min averaged data in the outflow flight segments to extrapolate back to the storm core top.
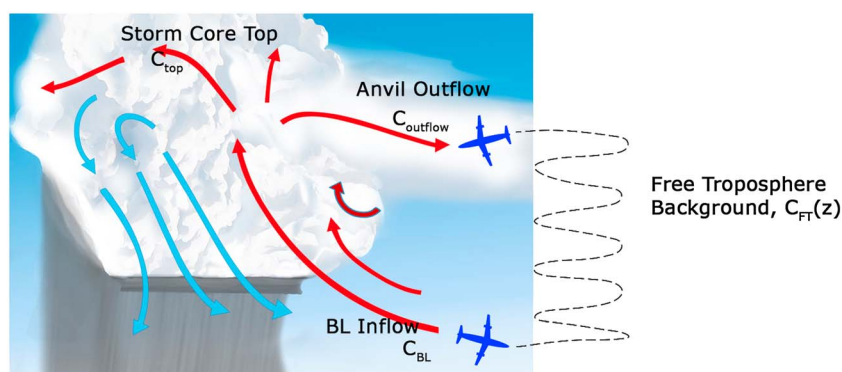

Figure 1. Air motions associated with deep convection in an environment with high vertical wind shear. The schematic is annotated with locations of the measured trace gas mixing ratios in the boundary layer inflow, free troposphere background, anvil outflow, and storm core top. Also shown is a schematic of the DC-8 flight pattern for sampling clear air profiles near the thunderstorm.
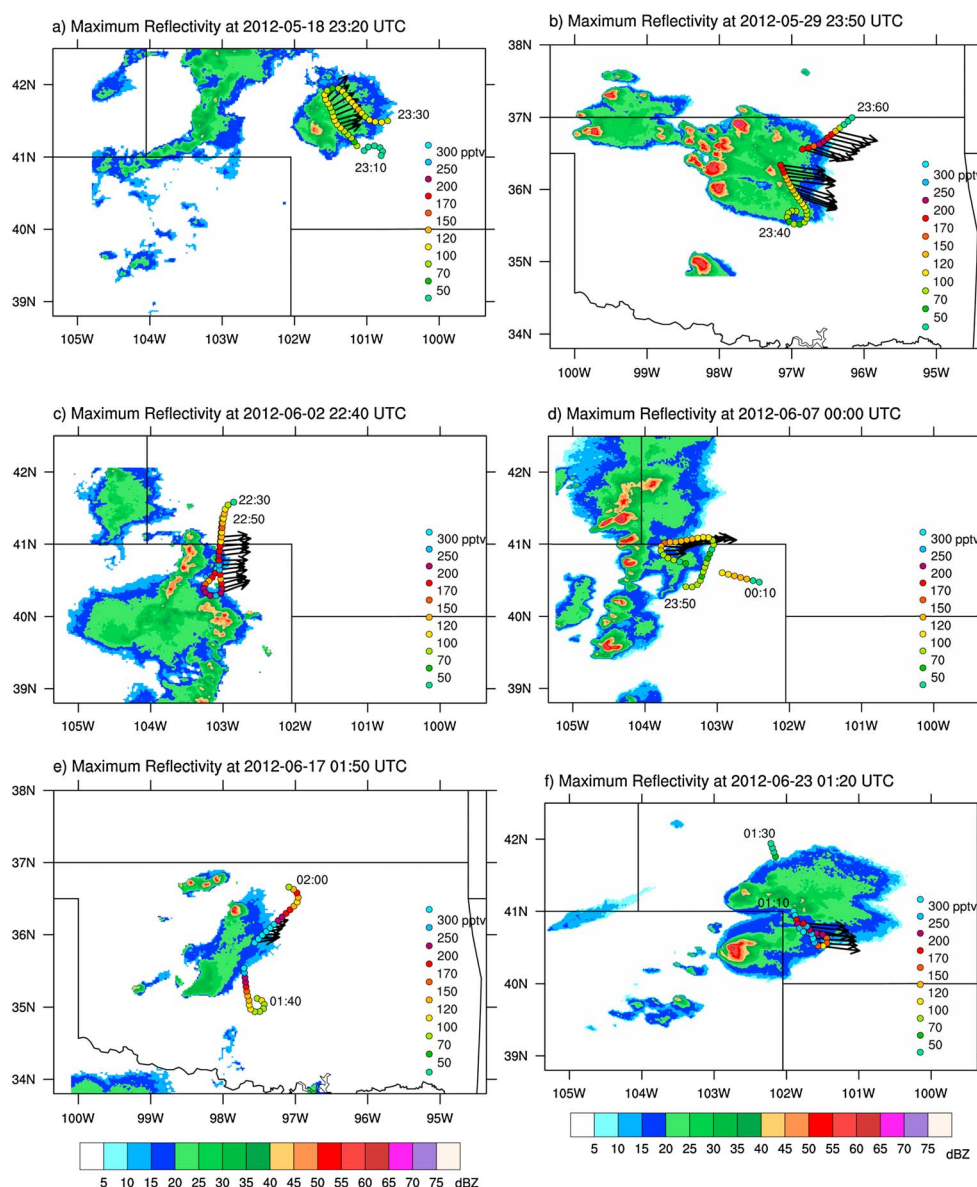
Figure 2. Maximum column reflectivity from the NWS NEXRAD radars for (a) 18 May southwest Nebraska, (b) 29 May Oklahoma, (c) 2 June Colorado, (d) 6 June Colorado, (e) 16 June Oklahoma, and (f) 22 June Colorado DC3 cases. Overlaid is the NASA DC-8 aircraft flight track with the start and end times of the flight leg and colored by the mixing ratio of CH_3OOH (pptv) for the 20 min surrounding the time of the radar reflectivity image. Vectors indicate the aircraft winds for times when outflow data were used for the scavenging efficiency calculation.

Aircraft sampling of the inflow and outflow regions was determined by identifying flight segments where horizontal winds showed air flowing into the storm within the boundary layer and air flowing away from the storm cores in the anvil, respectively. Besides the physical location of the aircraft, the chemical signatures of CO, hydrocarbons, and IWC were used to identify these flight legs. Figure 2 illustrates the outflow legs used in the analysis for the six convection cases. For each case, 20 min of the DC-8 flight track is plotted over the column maximum radar reflectivity. The DC-8 flight track is colored by the magnitude of the CH_3OOH 30 s averaged mixing ratio. The wind vectors (data from the MMS) are plotted for the segment of the flight track used for the outflow analysis. The inflow and outflow times and their altitudes for each of the cases are listed in Table 3. The inflow flight legs were within 1 km of the ground (the surface elevation for 18 May, 2 June, 6 June, and 22 June is ~1.5 km, and for 29 May and 16 June is ~0.5 km), obtaining a representative composition

Table 3. Inflow and Outflow Times (UTC) and Altitude (km and msl) of Measurements From the DC-8 Aircraft Used for Analysis

Date	Inflow Time (UTC)	Inflow Altitude (km)	Outflow Time (UTC)	Outflow Altitude (km)
18 May 2012	22:48:29–22:51:10	1.7	23:17:50–23:22:00	11.3
29 May 2012	23:10:21–23:15:53	1.3	23:49:18–23:58:13	11.0
02 June 2012	21:16:18–21:27:38	1.9	22:40:46–22:46:10	11.1
06 June 2012	22:13:40–22:25:12	1.7	23:57:22–24:01:59	12.4
16 June 2012	24:15:00–24:20:00	0.95	25:50:00–25:55:00	11.9
22 June 2012	22:31:27–22:45:54	2.0	25:16:51–25:19:24	11.2

of the boundary layer. The distance between the aircraft and storm cores varied among the different storm cases, with some cases (e.g., 29 May in Figure 2b) just a few kilometers from the cores developing in the anvil region and others (e.g., 22 June in Figure 2f) nearly 100 km from the storm core.

Once the inflow and outflow time periods were identified, the average mixing ratios for several trace gases were calculated. For the 18 May 2012 case, the inflow CH_3OOH mixing ratio was not available because of calibration or zeroing. The inflow value used for this case is taken from the lowest altitude (1.8 km) of the cloud-free data (discussed next). While not having the CH_3OOH mixing ratios during the inflow time period adds more uncertainty in the results for this case, we find for the other cases that the inflow CH_3OOH mixing ratios are within 20% of the lowest altitude cloud-free data average which is less than the uncertainties of the CH_3OOH mixing ratios.

To obtain information on air entraining into the storm, a vertical profile of cloud-free data from the storm region was obtained. Stratospheric air was omitted by removing times where the O_3 to carbon monoxide (CO) ratio was greater than 1.25 as was done by *Hudman et al.* [2007]. This method may not remove all of the data points with stratosphere influence because of mixing of air caused by the thunderstorms as described in recent studies [*Schroeder et al.*, 2014; *Huntrieser et al.*, 2016a, 2016b]. Also removed from these profiles were measurements of other unique features such as biomass burning plumes. These were removed by restricting the time frame for the profiles, which was determined from the high CO mixing ratios and the location of the aircraft to the smoke. Three flights had this restriction, described as follows. The 2 June cloud-free data were restricted to the 21:25 to 22:05 UTC time period when the aircraft spiraled up from the boundary layer to the upper troposphere. The 6 June cloud-free data were restricted to the 20:49 to 24:13 UTC time period in order to remove high concentrations from local emission sources in the Denver-Greeley area. The 22 June cloud-free data were restricted to the 22:00 to 25:40 UTC time period when the DC-8 aircraft was not intentionally sampling the High Park fire smoke plume. Most of the cloud-free profiles are based on the DC-8 spiral from the boundary layer to the upper troposphere and include the inflow data, but not the outflow data. The data were binned into 1 km altitude ranges. Missing data (because of in-flight calibrations or zeroing) were filled in by interpolating to the altitude of the missing data from the averages found above and below that altitude and extrapolating to the lowest or highest altitude, if needed. Figure 3 shows cloud-free vertical profiles of H_2O_2, CH_3OOH, *n*-butane, *i*-butane, *n*-pentane, and *i*-pentane for the six cases.

Cloud-free profiles of *n*-butane, *i*-butane, *n*-pentane, and *i*-pentane were used to estimate the entrainment rate. These VOCs have chemical lifetimes (3–5 days) much longer than the time for convective transport from the BL to the UT (typically 10–15 min) [*Skamarock et al.*, 2000] and transport downwind to the aircraft (typically 30–45 min). Long chemical lifetimes and very low solubility allow these VOCs to be markers of transport only. In addition, the butanes and pentanes generally have high mixing ratios in the BL and very low mixing ratios in the middle and upper troposphere. We will show that the contrast between the convective outflow region and the background UT for the butanes and pentanes is a factor of 3–12. On the other hand, the contrast of other candidate tracers is not quite as good. For example, CO varies between these regions by a factor of 1–1.35. While CO gives a much higher temporal resolution, the smaller contrast between outflow air and background UT makes it more difficult to use for entrainment rate calculations. The entrainment model follows an air parcel from just below cloud base (CB), where that air has a VOC mixing ratio representing the BL, to the location of the aircraft anvil measurements, where the VOC mixing ratio is a combination of the VOC from the BL and the cloud-free (CF)
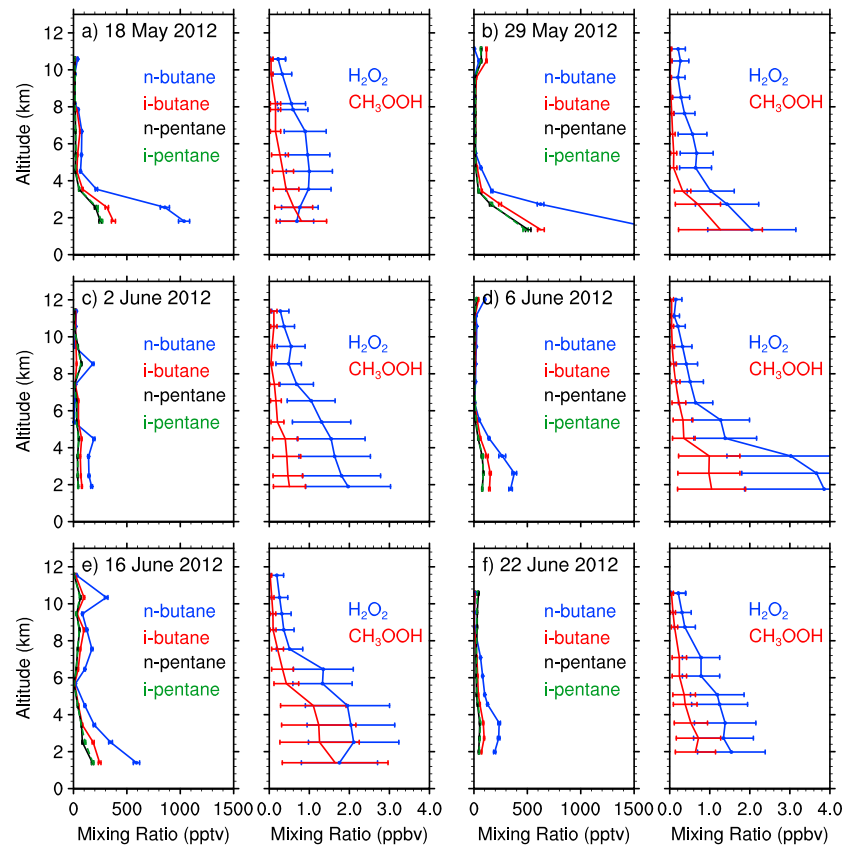
Figure 3. Cloud-free vertical profiles of *n*-butane (blue), *i*-butane (red), *n*-pentane (black), *i*-pentane (green), and H_2O_2 (blue) and CH_3OOH (red) for the (a) 18 May, (b) 29 May, (c) 2 June, (d) 6 June, (e) 16 June, and (f) 22 June 2012 DC3 cases. For butanes and pentanes, values plotted are averages and standard deviations of the averages or uncertainties based on measurement precision values (see text for more information). For peroxides, values plotted are averages and uncertainties based on measurement precision values.

VOC mixing ratios that are entrained into the storm. The entrainment rate E (% km^{-1}) is found by calculating the VOC mixing ratio at 1 km altitude bins from just below cloud base to the height of the aircraft measurements. For example, the VOC mixing ratio at one kilometer above cloud base (VOC(z_{CB+1})) is a combination of the VOC mixing ratio at cloud base (VOC(z_{CB})) and the VOC in the cloud-free air at one km above cloud base VOC$_{CF}$(z_{CB+1}) based on the fraction entrained. This equation can be generalized by the following equation:

$$VOC(z) = E \ VOC_{cf}(z) + (1 - E) \ VOC(z - 1) \tag{1}$$

where VOC(z) is the *n*-butane, *i*-butane, *n*-pentane, or *i*-pentane mixing ratio in the updraft at each 1 km altitude z (km), VOC(z-1) is the VOC mixing ratio at 1 km below the altitude z, and VOC$_{cf}$(z) is the average VOC mixing ratio in the cloud-free region at each 1 km altitude z. To determine E, equation (1) was iterated until the calculated VOC mixing ratio at the height of the aircraft outflow measurements and the measured VOC mixing ratio in the outflow region matched within 1–10%, which was determined based on a threshold mixing ratio connected to the measured outflow mixing ratio. This procedure was conducted for all four VOCs and the average entrainment rate was used to calculate the scavenging efficiency. The highest to lowest entrainment rates give the range of entrainment rates for each storm and are used in expressing the entrainment rate uncertainty. It is assumed that the entrainment rate is the same at every 1 km altitude; however, we estimate the impact of this assumption by utilizing variable entrainment rates determined in the WRF simulation for the 29 May DC3 case in section 3.

The first step in obtaining the scavenging efficiency of a soluble trace gas having mixing ratio C_{sol} is to determine C_{sol} at the height of the aircraft outflow measurements ($C_{sol}(z = top)$) if it were only transported (i.e., there is no dissolution into cloud particles and chemistry does not affect the mixing ratio of C_{sol}). C_{sol} $(z = top)$ is found by using equation (1) with H_2O_2 or CH_3OOH in place of the VOC and using the average entrainment rate. The scavenging efficiency SE (%) is found by calculating the difference between the soluble trace gas mixing ratio measured from the aircraft C_{sol} (outflow) and the estimated transported mixing ratio at the height of the aircraft C_{sol} $(z = top)$ using,

$$SE = 100 \frac{C_{sol}(z = top) - C_{sol}(outflow)}{C_{sol}(z = top)} \qquad (2)$$

The uncertainties in the scavenging efficiencies are found based on the uncertainties reported for the measurements in the aircraft data files and propagation of errors during the calculations of the estimated trace gas mixing ratio at storm top and the scavenging efficiency. The steps to getting the scavenging efficiency uncertainty are outlined here. The uncertainty δ for the inflow $\delta C_{sol}(inflow)$ and outflow $\delta C_{sol}(outflow)$ data as well as the 1 km binned cloud-free data $\delta C sol_{CF}(z)$, where z is the altitude, are the averages of the individual 1 s data uncertainties. Four entrainment rates are determined during the analysis, and the uncertainty of the average entrainment rate is the maximum difference between the average and highest or lowest entrainment rate. The uncertainty of the peroxide at the top of the storm core $\delta C_{sol}(z = top)$ is found from the entrainment rate equation, where the derivatives of the entrainment rate equation with respect to entrainment rate, cloud-free mixing ratio, and in-cloud mixing ratio are found at each altitude bin and are propagated upward to storm top. Lastly, the scavenging efficiency uncertainty is found by taking the derivatives of the scavenging efficiency equation with respect to $C_{sol}(outflow)$ and $C_{sol}(z = top)$ and combining these derivatives via propagation of errors [*Taylor*, 1982].

While equation (2) defines the scavenging efficiency, which is viewed as the physical removal of a trace gas via dissolution and rainout, the equation actually encompasses all physical and chemical processes occurring between the inflow and outflow regions sampled by the aircraft. Thus, there can be physical removal, chemical destruction, or even a reduction in chemical production. An example of the last process, mentioned in section 1 and discussed in section 4, is the reduction in peroxide formation because the peroxy radicals react with NO to form NO_2 and CH_2O instead of reacting with each other to form the peroxides.

2.3. Description of Cloud-Resolving Scale Model Simulations

The 29 May 2012 northern Oklahoma storm has been simulated with the Weather Forecasting and Research model coupled with Chemistry (WRF-Chem) [*Grell et al.*, 2005]. *Bela et al.* [2016] give a full description of the model configuration and simulation results. Table 4 provides information on the WRF-Chem configuration. The model domain is centered on northern Oklahoma using 1 km horizontal grid spacing and 88 vertical levels to 50 hPa (~20 km). The cloud resolving grid spacing allows for explicit representation of transport and wet deposition in the deep convection. The wet deposition scheme [*Neu and Prather*, 2012] estimates wet removal of soluble trace gases from the gas phase. This scheme estimates trace gas removal by multiplying the effective Henry's law equilibrium aqueous concentration by the net precipitation formation (conversion of cloud water to precipitation, minus evaporation of precipitation). In mixed-phase conditions ($258\,K < T < 273\,K$), the *Neu and Prather* [2012] scheme estimates a fraction of the dissolved gas to be retained in the frozen hydrometeors. The retention fraction of H_2O_2 and CH_3OOH is set to 0.64 and 0.01, respectively, in accordance with laboratory values compiled by *Leriche et al.* [2013]. Other soluble trace gases (CH_2O, HNO_3, and SO_2) also use retention factors recommended by *Leriche et al.* [2013], while all other trace gases are completely degassed from the condensed phase. Sensitivity simulations were conducted to explore the effect of the retention factor on trace gas scavenging.

In addition to the simulations that included wet deposition, a simulation without wet deposition was performed. The scavenging efficiencies (SE) are then calculated from these results using the following equation.

$$SE = 100 \frac{(C_{noscav} - C_{scav})}{C_{noscav}} \qquad (3)$$

where C_{noscav} and C_{scav} are average model mixing ratios of soluble trace gas C near the storm core as defined by the eastern (i.e., downwind) 40 dBZ maximum reflectivity contour. This location was chosen based on the

Table 4. Configuration of the WRF Simulation

Process	Parameterization	Reference
Meteorology initialization	North American Mesoscale Analysis with prestorm lightning data assimilation	*Fierro et al.* [2012]
Cloud microphysics	Morrison 2-moment	*Morrison et al.* [2009]
Deep/shallow convection	none	
Planetary boundary layer	YSU[a]	*Hong et al.* [2006]
Land surface	Noah	
Short/longwave radiation	RRTMG[b]	*Iacono et al.* [2008]
Chemistry initialization	Combination of aircraft measurements and MOZART global chemistry transport model	*Bela et al.* [2016] and *Emmons et al.* [2010]
Anthropogenic emissions	EPA NEI 2011	
Biogenic emissions	MEGAN[c] v2.04	*Guenther et al.* [2006]
Biomass burning emissions	FINN[d]	*Wiedinmyer et al.* [2011]
Gas-phase chemistry mechanism	MOZART[e]	*Emmons et al.* [2010]
Aerosol physics and chemistry	GOCART[f]	*Chin et al.* [2002]
Dry deposition	Resistance method	*Wesely* [1989]
Wet deposition	Henry's law equilibrium with net production of precipitation	*Neu and Prather* [2012]

[a]YSU = Yonsei University scheme.
[b]RRTMG = Rapid Radiative Transfer Model for GCMs.
[c]MEGAN = Model of Emissions of Gases and Aerosols from Nature.
[d]FINN = Fire Inventory from NCAR.
[e]MOZART = Model for Ozone and Related Chemical Tracers.
[f]GOCART = Goddard Chemistry Aerosol Radiation and Transport model.

analysis method of the observations outlined above. For the 29 May DC3 case, the DC-8 measurements were obtained near storm cores with reflectivity > 40 dBZ (Figure 2b). The mixing ratios of the trace gases were averaged in the convective outflow altitudes (9.43–11.59 km).

In another simulation, 20 tracers representing air in each 1 km altitude layer of the atmosphere from the surface to the top of the model (~20 km) are predicted. These layer tracers were set to a value of 1.0 in their respective layer for a 10 min time period (0010–0020 UTC 30 May 2012) and analyzed 2 h after the initialization of the tracer at 0200 UTC 30 May 2012 to allow time for boundary layer air to reach the outflow location. The tracers were analyzed to determine their percent contribution to the modeled storm outflow as defined above. The percent contributions (Table 5) are obtained by first calculating the fractional contribution of each tracer at each grid point then obtaining the average contribution of each tracer to the outflow region. Because of the averaging over the outflow region, the sum of the tracer contributions listed in Table 5 does not necessarily add to 100%. These percent contributions from each layer were used as the entrainment rate for calculations of scavenging efficiency from the aircraft observations to compare results from an average entrainment rate with those from an altitude-varying entrainment rate in section 3.

2.4. Box Model Calculations

The gas-aqueous chemistry box model described by *Barth et al.* [2003] is used to analyze the chemistry within the updraft regions of
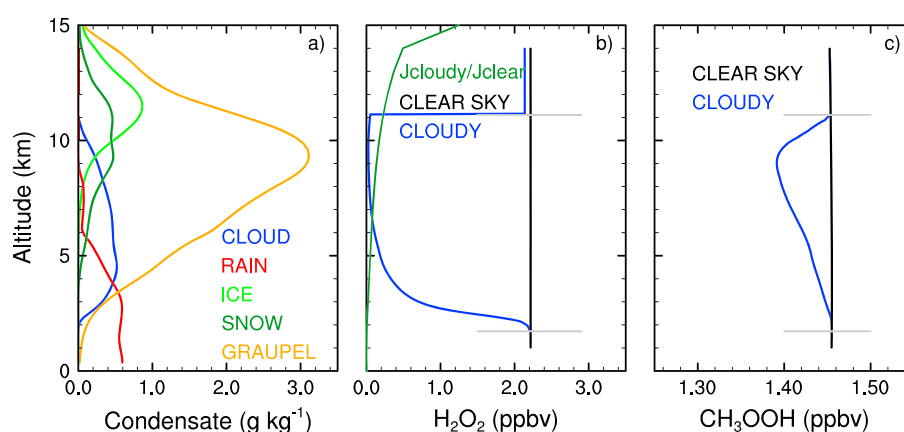
Table 5. Average Percent Contributions of Each 1 km Altitude Layer to the Storm Core Top as Determined From the WRF-Chem Simulation

Layer Bottom Altitude (km)	Layer Top Altitude (km)	Percent Contribution (%)
0	1	6.4 ± 4.8
1	2	12. ± 7.8
2	3	9.4 ± 5.5
3	4	5.0 ± 3.1
4	5	5.8 ± 3.6
5	6	8.5 ± 5.7
6	7	9.4 ± 6.7
7	8	8.4 ± 5.9
8	9	8.3 ± 7.9
9	10	5.7 ± 12.
10	11	0.26 ± 0.86
11	12	0.01 ± 0.02
Average for 1–11 km altitudes		7.3 ± 3.3

Figure 4. Vertical profiles of (a) storm hydrometeor mixing ratios obtained from the WRF-Chem simulation and gas-phase (b) H_2O_2 and (c) CH_3OOH mixing ratios calculated by the gas-aqueous photochemical box model. In Figure 4a, cloud water is the blue line, rain the red line, ice the green line, snow the dark green line, and graupel/hail the orange line. In Figures 4b and 4c, the gas chemistry only simulation is the black line, and the gas-aqueous chemistry is the blue line and used the cloud water mixing ratios shown in Figure 4a. The cloud water base and top are marked by the horizontal gray lines. In Figure 4b the ratio of the cloudy to clear-sky H_2O_2 photolysis rate at 00 UTC is shown in dark green.

a severe thunderstorm. The box model has been modified to include the nonmethane hydrocarbon gas-phase chemistry described by *Kim et al.* [2012]. The aqueous-phase chemistry represents only S(IV), O_3, H_2O_2, and CH_2O chemistry [*Barth et al.*, 2007a]. Other soluble VOC trace gases, e.g., organic aldehydes, peroxides, and nitrates, also partition into the aqueous phase following Henry's law equilibrium but do not undergo aqueous-phase chemistry. The coefficients for Henry's law are from *Sander* [2015] and *Sander et al.* [2011]. Photolysis rates are appropriate for 36°N beginning at 00 UTC (1900 local time), matching the time of the storm observations. The photolysis rates vary with altitude and are modified by cloud scattering assuming a cloud optical depth of 500, cloud base of 2 km, and cloud top of 15 km. The photolysis rates are less than their clear-sky values throughout the simulation as depicted by the cloudy to clear-sky H_2O_2 photolysis rate ratio in Figure 4b.

The box model has also been modified to have varying liquid water content, temperature, pressure, and altitude, which are prescribed using results from the WRF-Chem simulation during the mature phase of the simulated severe convective storm at 0000 UTC 30 May 2012. Values are averages at each model level within the 36°N–37°N and 99°W–97°W latitude and longitude region and where vertical velocity in the column exceeds 5 m s^{-1}. The resulting cloud hydrometeor vertical profiles are shown in Figure 4a. For the box model simulations we prescribe only the cloud liquid water content and exclude the water content from precipitation. From Figure 4, it is evident that much of the condensed water is in the precipitation, primarily as hail, for this updraft region. Because the box model calculations are a function of time, the prescribed time coordinate is converted to an altitude coordinate so that the chemistry of a hypothetical rising air parcel can be determined. The air parcel begins at the 1.16 km altitude (near cloud base), solves for only gas-phase chemistry for 10 min to allow the radicals to reach approximate photochemical equilibrium, then is lifted to higher altitudes assuming a 3 m s^{-1} updraft. At ~14 km where the WRF-Chem updraft velocities are ~0 m s^{-1}, the artificial lifting of the box is stopped. The 14 km altitude is above the cloud water region of the storm (Figure 4); the top of the cloud water region is 10.9 km. Thus, the air parcel undergoes only gas-phase chemistry between 10.9 and 14 km.

To determine if H_2O_2 and CH_3OOH would be depleted if only gas-phase chemistry were occurring, a box model simulation with no liquid water was performed. Figure 4 shows that H_2O_2 and CH_3OOH have similar mixing ratios at cloud top and cloud base (~2.2 ppbv for H_2O_2 and ~1.46 ppbv for CH_3OOH). Thus, for the conditions of the box model simulation, both peroxides are not produced by the gas-phase chemistry. A second simulation with the prescribed liquid water content shows that in the cloud water region (2–11 km altitude) gas-phase H_2O_2 is rapidly depleted, with mixing ratios reduced to <0.2 ppbv in the mixed cloud region (4–11 km altitude). Note that solubility constants increase as temperature decreases, allowing more of the

Table 6. Mixing Ratios of H_2O_2 and CH_3OOH (pptv) Averaged for the Inflow and Outflow Times and for the Cloud-Free Upper Troposphere Background[a]

Date	Inflow Time		Outflow Time		Background UT	
	H_2O_2	CH_3OOH	H_2O_2	CH_3OOH	H_2O_2	CH_3OOH
18 May	665 ± 407	803 ± 628[b]	87 ± 119	102 ± 71	221 ± 186	45 ± 48
29 May	2462 ± 1306	1522 ± 1276	169 ± 160	175 ± 104	210 ± 180	16 ± 37
02 June	2108 ± 1129	580 ± 459	60 ± 105	199 ± 109	277 ± 213	115 ± 78
06 June	4135 ± 2142	1148 ± 911	94 ± 122	126 ± 81	153 ± 151	48 ± 48
16 June	1777 ± 964	1655 ± 1381	90 ± 120	336 ± 164	189 ± 169	22 ± 39
22 June	1544 ± 847	647 ± 499	255 ± 203	276 ± 145	215 ± 183	43 ± 47

[a]The uncertainties of the average values are included.
[b]This value is from the lowest level of the cloud-free data.

soluble trace gas to partition into the aqueous phase. Gas-phase CH_3OOH mixing ratios also decrease, but by <10% of the gas-phase only simulation. At the top of the cloud water region, the peroxides in the aqueous phase return to the gas phase because of the lack of liquid water. In an actual cloud the cloud water is more likely being collected by precipitating cloud particles and freezing. Thus, what is shown in Figure 4 is akin to the trace gases being degassed from all cloud particles. In summary, simple partition theory based on Henry's law equilibria and gas- and aqueous-phase chemistry suggests substantial depletion of gas-phase H_2O_2 and small depletion of CH_3OOH. Gas-phase chemistry alone does not deplete either H_2O_2 or CH_3OOH appreciably during transit from cloud base to cloud top.

3. Results

Average mixing ratios for H_2O_2 and CH_3OOH measured during the DC-8 flight inflow and outflow time periods are listed in Table 6. The mixing ratios in the inflow region are always higher than those in the outflow for both peroxide species, indicating that net chemical production of peroxides within the storm is not occurring at rates greater than the rate of dilution. The inflow mixing ratios vary from case to case, suggesting a dependence on vicinity to anthropogenic sources and time of year. The 18 May and 22 June storms, with lower H_2O_2 mixing ratios, both occurred near the Wyoming-Colorado-Nebraska border farther from the Front Range urban region than the 2 and 6 June Colorado cases. The outflow mixing ratios also have some variability among the different storm cases. Four of the cases have H_2O_2 outflow mixing ratios below 100 pptv, which is near the offset of the H_2O_2 uncertainty (=75 pptv), suggesting substantial scavenging of H_2O_2. Average H_2O_2 and CH_3OOH mixing ratios for the background UT region, which represent the highest altitude of the cloud-free vertical profile (Figure 3), are also listed in Table 6. A comparison of the outflow peroxide mixing ratios to the background UT shows that the outflow H_2O_2 is always less than the background UT, on average, while the outflow CH_3OOH is always greater than the background UT, on average. The uncertainties for the average values can be quite large, ranging from 50 to 60% and from 77 to 84% for H_2O_2 and CH_3OOH, respectively, in the boundary layer inflow air, 80 to 175% and 49 to 70% for H_2O_2 and CH_3OOH, respectively, in the outflow air, and 77 to 99% and 68 to 230% for H_2O_2 and CH_3OOH, respectively, in the background UT.

The mixing ratios for the butanes and pentanes in the inflow air (Table 7) vary from storm to storm, where higher mixing ratios in both the inflow and outflow air occur over Oklahoma (29 May and 16 June cases) compared to those in Colorado, except for the 18 May case. The outflow mixing ratios are often much smaller than the inflow mixing ratios, except for the 22 June outflow where mixing ratios are only slightly less than those in the inflow suggesting less entrainment occurred during transport from the boundary layer to the location of the aircraft in the anvil in the 22 June storm. Note that the number of canisters varied from 1 to 4 for representing inflow and 1 to 2 for outflow air. While there is only one outflow sample for the 22 June case, its neighboring canister samples, taken in another part of the outflow region, had similar butane and pentane mixing ratios. The 6 June case uses butane and pentane mixing ratios extrapolated to the storm top as determined by A. Fried et al. (submitted manuscript, 2016) because the DC-8 mixing ratios from the outflow period listed in Table 5 have anomalously high butane and pentane mixing ratios that are greater than the inflow mixing ratios. Instead of using DC-8 data from outflow near the edge of the storm (and quite far from the

Table 7. Mixing Ratios of *n*-Butane, *i*-Butane, *n*-Pentane, *i*-Pentane (pptv) Averaged for the Inflow and Outflow Regions and for the Cloud-Free Upper Troposphere Background[a]

Date	Inflow Region[b]		Outflow Region[c]		Background UT	
	n-butane	*i*-butane	*n*-butane	*i*-butane	*n*-butane	*i*-butane
18 May	1511 ± 75	537 ± 27	431 ± 65	164 ± 23	38 ± 3	19 ± 3
29 May	1548 ± 77	513 ± 26	763 ± 61	280 ± 25	5 ± 3	23 ± 4
02 June	262 ± 68	112 ± 25	108 ± 5	51 ± 3	27 ± 3	21 ± 3
06 June	312 ± 28	132 ± 10	224 ± 34[d]	95 ± 14[d]	102 ± 5	42 ± 3
16 June	1746 ± 514	678 ± 165	406 ± 39	169 ± 19	29 ± 3	19 ± 3
22 June	194 ± 25	70 ± 11	150 ± 8	52 ± 3	10 ± 3	9 ± 3
	n-Pentane	*i*-Pentane	*n*-Pentane	*i*-Pentane	*n*-Pentane	*i*-Pentane
18 May	365 ± 18	377 ± 19	107 ± 17	110 ± 18	13 ± 3	11 ± 3
29 May	457 ± 22	397 ± 20	202 ± 17	210 ± 26	68 ± 5	65 ± 5
02 June	68 ± 19	73 ± 25	31 ± 3	32 ± 3	14 ± 3	7 ± 3
06 June	80 ± 8	84 ± 13	56 ± 8[d]	54 ± 8[d]	25 ± 3	23 ± 3
16 June	596 ± 202	550 ± 145	105 ± 21	109 ± 18	7 ± 3	8 ± 3
22 June	44 ± 4	49 ± 5	42 ± 3	34 ± 3	43 ± 3	31 ± 3

[a]The standard deviations of the averages, or uncertainties based on measurement precision values, are included.
[b]The number of canister samples used for each of the inflow periods is 1 for 18 May and 29 May, 2 for 16 June, 3 for 2 June and 22 June, and 4 for 6 June.
[c]The number of canister samples used for each of the outflow periods are 2 for 18 May, 29 May, 2 June, and 16 June cases, and 1 for 22 June. See text for discussion of the 6 and 22 June samples.
[d]Values from A. Fried et al. (submitted manuscript, 2016) using the outflow measurements from both the DC-8 and GV. These values are extrapolated to the top of the storm core as described by A. Fried et al. (submitted manuscript, 2016).

storm cores), we chose to use the mixing ratios determined from a combination of DC-8 and GV data (A. Fried et al., submitted manuscript, 2016). Average butane and pentane mixing ratios for the background UT region, which represent the highest altitude of the cloud-free vertical profile (Figure 3), are also listed in Table 7. A comparison of the outflow to the background UT mixing ratios shows that the background UT butanes and pentanes are 3–15 times less than the outflow region, on average.

The *i*-butane/*n*-butane and *i*-pentane/*n*-pentane ratios also provide evidence that the air measured by the DC-8 in the inflow region of the storms is connected to that sampled in the outflow region in the storm anvils. *Gilman et al.* [2013] and *Swarthout et al.* [2013] explain that these ratios are limited to a small range of values for a given source (e.g., cities, biomass burning emissions, and oil and gas emissions). However, the ratios from source to source vary, where the *i*-butane/*n*-butane ratio is found to be 0.48 for U.S. cities, 0.26–0.27 for biomass burning emissions, 0.36–0.69 for oil and gas emissions, and *i*-pentane/*n*-pentane ratio is 2.0 for U.S. cities, 0.31–0.37 for biomass burning emissions, and 1–1.4 for oil and gas emissions in the Texas, Oklahoma, Kansas region (N. J. Blake et al., Spatial distributions and source characterization of trace organic gases during SEAC4RS and comparison to DC3, in preparation, 2015; A. Fried et al., submitted manuscript, 2016). These ratios should be maintained for several hours because their rate constants with OH are within 10–15% for *n*-butane and *i*-butane oxidation and within 10% for *n*-pentane and *i*-pentane oxidation. The *i*-butane/*n*-butane and *i*-pentane/*n*-pentane ratios for the inflow regions of all the storms analyzed for this study lie within the range for oil and gas emissions as found by N. J. Blake et al. (in preparation, 2015) and *Gilman et al.* [2013] for the Texas, Oklahoma, and Kansas region (Table 8). This is not a surprising result because both Oklahoma and northeast Colorado have active oil and gas operations.

Table 8. The *i*-Butane/*n*-Butane and *i*-Pentane/*n*-Pentane Ratios Averaged for the Inflow and Outflow Regions[a]

Date	Inflow	Outflow	Inflow	Outflow
	i-Butane/*n*-Butane		*i*-Pentane/*n*-Pentane	
18 May	0.36	0.38	1.03	1.03
29 May	0.33	0.37	0.87	1.04
02 June	0.43	0.47	1.06	1.03
06 June	0.42	0.42	1.05	0.96
16 June	0.39	0.42	0.92	1.04
22 June	0.36	0.35	1.11	0.81

[a]Values in the outflow region of 6 June storm are from A. Fried et al. (submitted manuscript, 2016) who used the outflow measurements from both the DC-8 and GV and extrapolated to the top of the storm core.

Table 9. Entrainment Rate and Scavenging Efficiencies for Each Storm Analyzed

Date	Entrainment Rate (% km^{-1})	Scavenging Efficiencies (%)	
		H$_2$O$_2$	CH$_3$OOH
18 May 2012	13.2 ± 0.2	85 ± 21	68 ± 28
29 May 2012	7.6 ± 1.6	88 ± 11	77 ± 20
02 June 2012	16.5 ± 4.6	94 ± 13	12 ± 67
06 June 2012	4.1^a ± 0.7	97 ± 05	84 ± 15
16 June 2012	17.2 ± 1.7	89 ± 15	30 ± 50
22 June 2012	4.8 ± 0.9	79 ± 19	44 ± 47

^{a}Entrainment rate is from A. Fried et al. (submitted manuscript, 2016).

The *i*-butane/*n*-butane and *i*-pentane/*n*-pentane ratios are fairly consistent between inflow air and outflow air for each storm, although some differences occur possibly because the storm is entraining air with different *i*-butane/*n*-butane and *i*-pentane/*n*-pentane ratios than the inflow region. Nevertheless, these ratios indicate that the two air masses sampled are well connected between inflow and outflow of each storm.

Entrainment rates, as calculated via the method described in section 2.2, range from 4.1% km^{-1} to 17.2% km^{-1} for the different storms analyzed (Table 9). The entrainment rate for 6 June was obtained from A. Fried et al. (submitted manuscript, 2016) because the VOCs measured by the DC-8 were anomalously high in the outflow region. The entraining rates for three of the cases are similar to those found by *Luo et al.* [2010] who used moist static energy profiles to determine entrainment rates of <10% km^{-1} for deep convective tropical, oceanic cumulus clouds. Moreover, the entrainment rate for the 29 May storm is identical to that found by A. Fried et al. (submitted manuscript, 2016). The entrainment rate for the 22 June storm is within the mutual precision limits of A. Fried et al. (submitted manuscript, 2016) who estimated 3.1 ± 1.1% km^{-1} compared to 4.8 ± 0.9% km^{-1} in this study. The small difference for the 22 June storm is expected since A. Fried et al. (submitted manuscript, 2016) extrapolate their outflow data to estimate mixing ratios at storm core top, which are generally higher than the average values closest to the storm core employed here. If the entrainment rates reported in Table 9 are integrated over a 9 km depth, the total storm entrainment rate range for the storms with high 0–6 km vertical wind shear and high CAPE (Table 2) is 40–68%, which is similar to entrainment rates of midlatitude, continental convection [*Barth et al.*, 2007a; *Thompson et al.*, 1994], and subtropical convection [*Scala et al.*, 1990]. Both low-level vertical wind shear and entrainment rate contribute to the storm intensity and longevity, as they play a role in the strength of the cold pool and tilt of the updraft [*Weisman et al.*, 1988; *Lee et al.*, 2008]. The storms with higher entrainment rates per kilometer have integrated entrainment rates of >100%. By examining the cloud-free profiles, air ingested 1–2 km above the inflow flight leg is also in or just above the BL. Air from these regions have also been documented as being major sources of inflow air [*Cotton et al.*, 1995; *Scala et al.*, 1990].

The calculated scavenging efficiencies for H$_2$O$_2$ and CH$_3$OOH for each storm analyzed range from 79% to 97% and 12% to 84%, respectively (Table 9). While there is some variability of scavenging efficiency among storms for H$_2$O$_2$, there is much more variability for CH$_3$OOH. The H$_2$O$_2$ scavenging efficiencies estimated from DC3 storms are somewhat greater than those previously found. Numerical modeling of a low-precipitation supercell observed in northeast Colorado yielded a 57% H$_2$O$_2$ scavenging efficiency [*Barth et al.*, 2007a]. *Wang* [2005] estimated H$_2$O$_2$ scavenging efficiencies of 88–90% for tropical deep convection. Global chemistry transport model simulations estimated that a soluble species with a Henry's law coefficient similar to H$_2$O$_2$ has a 90% scavenging efficiency in deep convection [*Crutzen and Lawrence*, 2000]. Estimated H$_2$O$_2$ scavenging efficiency, based on boundary layer, convective outflow, and UT background observations for an oceanic, tropical convective storm is 55–70% [*Cohan et al.*, 1999]. CH$_3$OOH scavenging efficiencies for DC3 storms are also greater than past results. *Barth et al.* [2007a] determined a 7% scavenging efficiency, while *Cohan et al.* [1999] found no significant scavenging of CH$_3$OOH.

It is important to realize that the uncertainty in the estimated scavenging efficiencies is large and is mostly a product of the uncertainties of the peroxide measurements. The peroxide uncertainties for low altitude are 52–61% for H$_2$O$_2$ and 77–84% for CH$_3$OOH and for high altitude are 80–175% for H$_2$O$_2$ and 49–70% for CH$_3$OOH (Table 6). Examining the impacts of the CH$_3$OOH uncertainties was done by testing lower BL CH$_3$OOH mixing ratios with higher outflow mixing ratios. Previous studies have found BL CH$_3$OOH to be 400–600 pptv [*Snow et al.*, 2007; *Barth et al.*, 2007a] over North America. When CH$_3$OOH = 500 pptv is the BL mixing ratio entering the cloud for the 6 June case (using the 4.1% km^{-1} entrainment rate), the CH$_3$OOH scavenging efficiency is 62% for the average CH$_3$OOH outflow mixing ratio of 126 pptv and 37% for the average + uncertainty CH$_3$OOH outflow mixing ratio of 207 pptv. These scavenging efficiencies extend

beyond the reported 6 June uncertainty but are still much greater than the expected scavenging efficiency of <10% based on previous studies. The high uncertainties propagate to the scavenging efficiencies, manifesting into 5–25% relative uncertainty (= uncertainty/average) in the H_2O_2 scavenging efficiency and 18–558% relative uncertainty in the CH_3OOH scavenging efficiency. For CH_3OOH, there tends to be more uncertainty associated with the lower scavenging efficiencies.

In addition to the measurement uncertainties, there are uncertainties associated with the analysis method. While much care was invested in quantifying relevant values in inflow and outflow air, there exists the possibility that the times chosen include air that was not processed by the deep convection. However, by using the 1 s data, we expect air from outside the anvil to have very little influence on the calculated average outflow mixing ratios. Further, comparison of the i/n butane and i/n pentane ratios give good information on how well the boundary layer and outflow air are connected. A major assumption of the analysis is that the entrainment rate is constant for each kilometer layer from cloud base to the top of the storm cell. To test this assumption, the WRF-Chem model run using tracers described in section 2.3 was analyzed to provide an altitude-dependent entrainment rate (Table 5) for the 29 May severe convection case in Oklahoma. For this case, the entrainment rate based on the hydrocarbon analysis was estimated to be 7.6% km^{-1}, while the WRF-Chem model estimated an average percent contribution from each 1 km altitude layer over the 1–11 km altitude range to be 7.3%. Thus, the average entrainment rates based on these two methods are similar. However, the model results give a variation of contributions with height, with higher entrainments rates per km in the first 2 km (near cloud base) and near 7 km, and the lowest entrainment rates per kilometer between 3 and 5 km altitude and above 9 km altitude (Table 5). By using the altitude-dependent entrainment rates for estimating the scavenging efficiency, we obtain values of 89% and 80% scavenging for H_2O_2 and CH_3OOH, respectively. These values are similar to the 88% and 77% estimated by the constant entrainment rate method and are well within the uncertainty.

The most surprising result is the substantial scavenging of CH_3OOH for two of the storms (29 May and 6 June) of greater than 75%, which is much greater than what is expected based on Henry's law equilibrium between the gas and aqueous phases (section 2.4), even when the uncertainties for these high scavenging efficiencies are considered (i.e., the average minus the uncertainty gives scavenging efficiencies much greater than expected). However, the cloud physics in deep convective clouds is much more complicated than the simple model of a liquid-only cumulus cloud. The ice phase in deep convection interacts with the cloud and rain drops through freezing and melting processes, and the fate of the dissolved trace gas is uncertain when freezing occurs [*Barth et al.*, 2001, 2007a] but is related to the value of the trace gas Henry's law and the time it takes a drop to freeze [*Stuart and Jacobson*, 2006]. Other storm characteristics (e.g., entrainment) can also affect the scavenging rate of the trace gas. Some of these effects will be discussed in the next section.

A comparison of WRF-Chem simulations with and without wet deposition was done to estimate scavenging efficiencies for the 29 May northern Oklahoma storm. Average H_2O_2 and CH_3OOH mixing ratios at the eastern edge of the modeled storm core tops, which was defined in longitude-latitude space by the column maximum radar reflectivity of 40 dBZ, were found for each of the simulations. *Bela et al.* [2016] explore the sensitivity of the scavenging efficiency to the retention of the dissolved trace gas in freezing drops. They find the H_2O_2 scavenging efficiency to be 100% with retention fractions into ice of 0.25, 0.5, 0.64, and 1.0 and 78 ± 11% when there is no retention of dissolved trace gas in freezing drops. For CH_3OOH, *Bela et al.* [2016] find the scavenging efficiency to be 26 ± 6%, 35 ± 7%, 39 ± 5%, 51 ± 4%, and 61 ± 3% for retention fractions of 0, 0.02, 0.25, 0.5, and 1.0, respectively. The model results with 100% retention for CH_3OOH in ice give a CH_3OOH scavenging efficiency (61%) most similar to the value calculated from observations (77%). In contrast, the simulation with 0% retention in ice produced CH_2O mixing ratios in the convective outflow that best matched the observations (A. Fried et al., submitted manuscript, 2016). Further analysis is being done to investigate the potential role of aqueous-phase chemistry on peroxide mixing ratios. These results suggest the retention of H_2O_2 and CH_3OOH in freezing drops is an important contribution to scavenging of peroxides.

4. Discussion

Here we seek to get an idea of what atmospheric processes contribute to the wide range of CH_3OOH scavenging in order to guide future analyses. We first compare the 2 and 6 June cases because of their very different

CH_3OOH scavenging efficiencies for two storms that developed in northeast Colorado just a few days apart. To do a thorough study of each storm individually would mean diagnosing the cloud physics processes and chemical transformations within the storm. While some of the cloud physics characterization can be estimated from the polarimetric radar data, cloud chemistry modeling would provide more detailed analysis of the physical and chemical processes. Such modeling has begun with the 29 May Oklahoma storm [*Bela et al.*, 2016]. Here we discuss the meteorological and chemical settings, in which the 2 and 6 June storms formed and discuss some differences between the storms that we determined using NEXRAD data. We then expand upon the discussion by examining correlations between different storm parameters and the CH_3OOH scavenging efficiencies for all six storms.

4.1. Comparison of the 2 and 6 June Storm Cases

The 2 and 6 June storms occurred in a very similar location, near the Wyoming-Colorado-Nebraska border (Figures 2c and 2d). Both days had several storms occurring in the region, making it challenging to attribute the outflow sampling to one specific storm. However, the synoptic meteorological conditions differ between the cases. In response to an upper level wave, the 2 June storms began in the late morning over the higher mountainous terrain and propagated eastward over the High Plains of Colorado and Wyoming. The 6 June storms began as a result of the Denver cyclone, where southeasterly low-level flow meets northwesterly flow from the west of Denver. The first storm appeared at the apex of the cyclone, which was northeast of Denver. Subsequently, as a cold front entered northeastern Colorado, storms formed closer to the foothills of Colorado and Wyoming propagating eastward. At the time of outflow sampling, the storms for both 2 and 6 June were mature multicell lines of convection (Figure 2).

The thermodynamic environment is critical for determining storm morphology and intensity. Two important parameters of the thermodynamic environment are the convective available potential energy (CAPE) and the low-level vertical wind shear [*Weisman and Klemp*, 1982]. The storm environment is analyzed using the soundings from the NCAR Mobile GPS Advanced Upper-Air Sounding System. A comparison of the storm environment parameters derived from the soundings (Table 2) reveals that the CAPE was substantially different between the two days. Although the 2 June sounding is from 1700 UTC, more than 5 hours before the convective outflow was sampled, the cloud-free aircraft measurements show a similar temperature and dew point vertical profile, but with a deeper boundary layer (reaching 4 km mean sea level (msl), which is also the height of the cloud base according to the radiosonde). On 6 June, the cloud base height was ~3.5 km msl altitude (~2 km aboveground). The vertical profile of the water vapor mixing ratios measured by the DC-8 aircraft and radiosondes shows that there is more water in the lower atmosphere on 6 June that is capped by relatively drier air in the midtroposphere. In contrast, water vapor in the cloud-free upper troposphere (above 7 km) is greater on 2 June compared to 6 June. Because of the higher cloud base on 2 June, the depth of the liquid water region (cloud base to the freezing level and cloud base to $T = -40°C$) was shallower on 2 June compared to 6 June. The difference in the depth of the liquid water region may be important for CH_3OOH scavenging, especially in terms of collection of cloud drops by hail or graupel. That is, there may be more CH_3OOH scavenged because there is a bigger region for drop collection. If hail plays an important role in the scavenging of CH_3OOH, its recirculation up and down in the storm may be the reason more CH_3OOH is removed.

High radar reflectivity regions are associated with larger precipitation particles including rain, graupel, and hail. To examine the possible role of graupel and hail, the volume of the region exceeding 35 dBZ from the NEXRAD reflectivity was computed for each storm. These volumes were calculated for when the air parcel, which was sampled by the aircraft, exited the storm core top. For 2 June this time interval is 30 min; thus, 22:10 NEXRAD data were used. For 6 June the time interval is ~60 min; thus, 23:10 NEXRAD data were used. For both cases, between the time of the 35 dBZ volume calculation and the time of the outflow sample, new storm cores developed in the region complicating the analysis. The estimated 35 dBZ volumes for 2 June was 3652 km^3 for three storm cores, while for 6 June it was 2474 km^3 for two storm cores. Thus, the 2 June storm had a larger volume than the 6 June case, suggesting that there was more graupel and hail in the 2 June case. Although this result may seem counter to the hypothesis that more graupel or hail increases the scavenging of trace gases, the 35 dBZ volume per storm core was about the same. Further analysis of graupel and hail amounts using the polarimetric radar data can reveal whether wet growth riming forming hail is more important than dry growth riming forming graupel. This type of analysis is beyond the scope of this paper, which is to highlight the higher than expected CH_3OOH scavenging efficiencies and suggest possible causes.
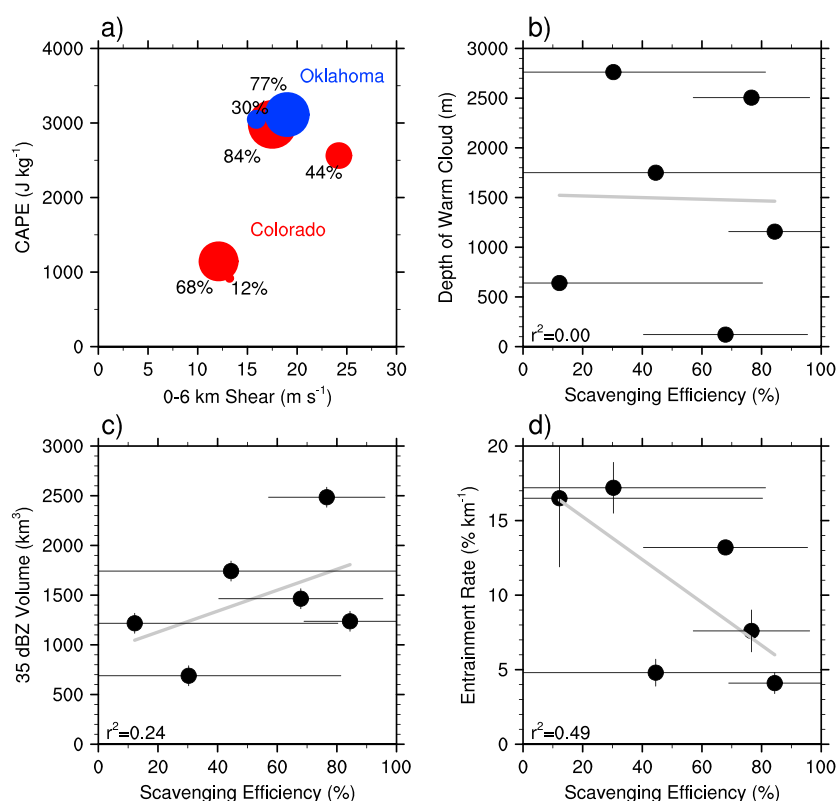
Figure 5. (a) Scavenging efficiencies of CH_3OOH placed in the CAPE—low-level vertical wind shear parameter space. The size of the circles is scaled to the scavenging efficiency values. Blue circles denote Oklahoma storms, and red circles are Colorado storms. Correspondence of estimated CH_3OOH scavenging efficiencies and (b) depth of the warm cloud defined as from cloud base to the freezing level, (c) volume of the 35 dBZ region normalized to the number of storm cores, and (d) storm entrainment rates. The gray line in each plot represents the regression line for the data shown.

The derived entrainment rate of $16.5 \pm 4.6\%\,km^{-1}$ for the 2 June and $4.1 \pm 0.7\%\,km^{-1}$ for the 6 June storms are very different (Table 9). Although CH_3OOH mixing ratios in the lowest 4 km msl cloud-free air for the 6 June case are about twice those for the 2 June case (Figure 3), the 6 June case entrains substantially less CH_3OOH from outside the storm. The lower entrainment rate allows more BL air to reach the top of the storm, creating a greater difference between the expected transported trace gas and the measured outflow trace gas mixing ratios. The entrainment of moister air into the storm on 2 June may also be affecting the cloud microphysical processes that subsequently affect CH_3OOH scavenging.

Chemical transformations may also play a role, as will be discussed in more detail in the next section. The composition of the inflow regions for 2 and 6 June were fairly similar. On 2 June, O_3, CO, and NO_x in the inflow region were 54 ppbv, 110 ppbv, and 565 pptv, while on 6 June O_3, CO, and NO_x in the inflow region were 61 ppbv, 125 ppbv, and 435 pptv. The higher CO on 6 June was also in line with slightly higher CH_2O on 6 June (1.61 ppbv) compared to 2 June (1.50 ppbv). However, inflow SO_2 mixing ratios differed on the two days. On 2 June SO_2 was 745 pptv in the inflow region, while on 6 June SO_2 was 98 pptv. Since CH_3OOH reacts with S(IV) in the aqueous phase, this difference in inflow SO_2 may further impact CH_3OOH scavenging efficiencies.

In summary, while the 2 and 6 June storm cases are similar in that they occur in the same region within a few days, the formation of the storms was different in that the 2 June storms began over the high terrain to the west, while the 6 June storms formed over the High Plains of Colorado. Differences between characteristics of the 2 and 6 June cases that may affect the CH_3OOH scavenging efficiencies are the storm environment CAPE, the entrainment rate, the depth of the liquid water region, the amount of graupel and/or hail, and the inflow SO_2 mixing ratio because of its reaction with CH_3OOH in the aqueous phase. These parameters are examined further in the context of all six storms analyzed.

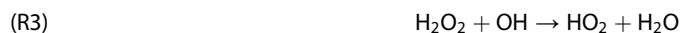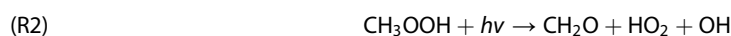### 4.2. Correlations of Parameters Among All Six Storm Cases

In this section, possible factors influencing the CH_3OOH scavenging efficiencies are studied further to see if differences highlighted by the 2 and 6 June storm comparison show a correspondence for all six storm cases. While the 2 and 6 June storms had very different CAPE, placing the CH_3OOH scavenging efficiencies in the context of the thermodynamic environment (Figure 5a) shows that there is no strong correlation of CH_3OOH scavenging efficiencies with CAPE and the 0–6 km vertical wind shear, although the two highest CH_3OOH scavenging efficiencies occur in severe storms with similar CAPE and vertical wind shear parameters.

In the previous section, we showed that the depth of the warm cloud (between cloud base and the freezing level) where only liquid water resides was shallower for the 2 June case, which had a 12% CH_3OOH scavenging efficiency, than for the 6 June case with an 84% scavenging efficiency. However, when all six cases are examined, we find no correlation between the CH_3OOH scavenging efficiency and the depth of the warm cloud (Figure 5b), suggesting that the ice-liquid processes (e.g., retention of dissolved gases during cloud drop freezing) impacts the scavenging efficiency. Supercooled liquid water can exist at temperatures down to 233 K ($-40°C$), and dissolution into the liquid from the gas phase occurs much more readily at colder temperatures. Nevertheless, the calculated CH_3OOH scavenging efficiencies showed no correlation with the depth of cloud where cloud droplets exist. Thus, the size of the region for dissolution of trace gases and precipitation formation is not important for peroxide scavenging.

To further examine the connection between CH_3OOH scavenging efficiencies and graupel and hail, we calculated the 35 dBZ volume from the NEXRAD data at the time estimated for when the air parcels exited the top of the storm cores. In some storm cases, more than one storm core contributed to the outflow region. Therefore, we have normalized the 35 dBZ volume by the number of storm cores. Figure 5c shows that there is some correspondence between the normalized 35 dBZ volumes and the CH_3OOH scavenging efficiencies with $r^2 = 0.24$. This result suggests that future studies examine further the role of the graupel and hail physics on CH_3OOH scavenging.

As shown in the comparison between the 2 and 6 June storms, the entrainment rates are very different and could explain why there are differences in scavenging efficiencies between storms. When examining all six storms, the increase in scavenging efficiency with a decrease in entrainment is still seen and has a moderate correlation (Figure 5d). As stated above, a lower entrainment rate allows more BL air to reach the top of the storm, creating a greater difference between the expected transported trace gas and the measured outflow trace gas mixing ratios when the trace gas has higher mixing ratios in the boundary layer compared to the middle and upper troposphere. The possible importance of entrainment on convective outflow mixing ratios suggests that the shape of the vertical profile of the peroxides may be important. For example, a rapid decrease in mixing ratio from the top of the boundary layer into the free troposphere would decrease CH_3OOH more than if the cloud-free mixing ratios remained elevated into the midtroposphere (e.g., 16 June, Figure 3).

Another factor to consider is the chemistry that the peroxides experience as they are transported from cloud base to the aircraft location in the anvil outflow region. Both H_2O_2 and CH_3OOH are primarily destroyed by photolysis ((R1) and (R2)) and oxidation by OH ((R3) and (R4)).

(R1) $$H_2O_2 + hv \rightarrow 2\,OH$$

(R2) $$CH_3OOH + hv \rightarrow CH_2O + HO_2 + OH$$

(R3) $$H_2O_2 + OH \rightarrow HO_2 + H_2O$$

(R4) $$CH_3OOH + OH \rightarrow products$$

The rates of these reactions are altered by the presence of deep convection because the cloud particles scatter incoming solar radiation. When the cloud attenuates solar radiation causing reduced photolysis rates and OH concentrations [*Chang et al.*, 1987; *Brasseur et al.*, 2002], the photochemistry tends to proceed more slowly. However, near the top of cloud where it is much brighter, the chemistry is accelerated. Because H_2O_2 and CH_3OOH are both produced and destroyed by HO_x and photolysis rates, their gas-phase photochemistry is less certain when clouds scatter radiation. Previous modeling studies showed a <5% effect on peroxide mixing ratios caused by cloud modified photolysis rates for boundary layer clouds in a marine setting [*Barth et al.*, 2002]. However, *Wang* [2005] expected increases of H_2O_2 in the upper regions of deep convection due to the decreased photolysis rates and lack of water in which H_2O_2 dissolves and undergoes aqueous chemistry.
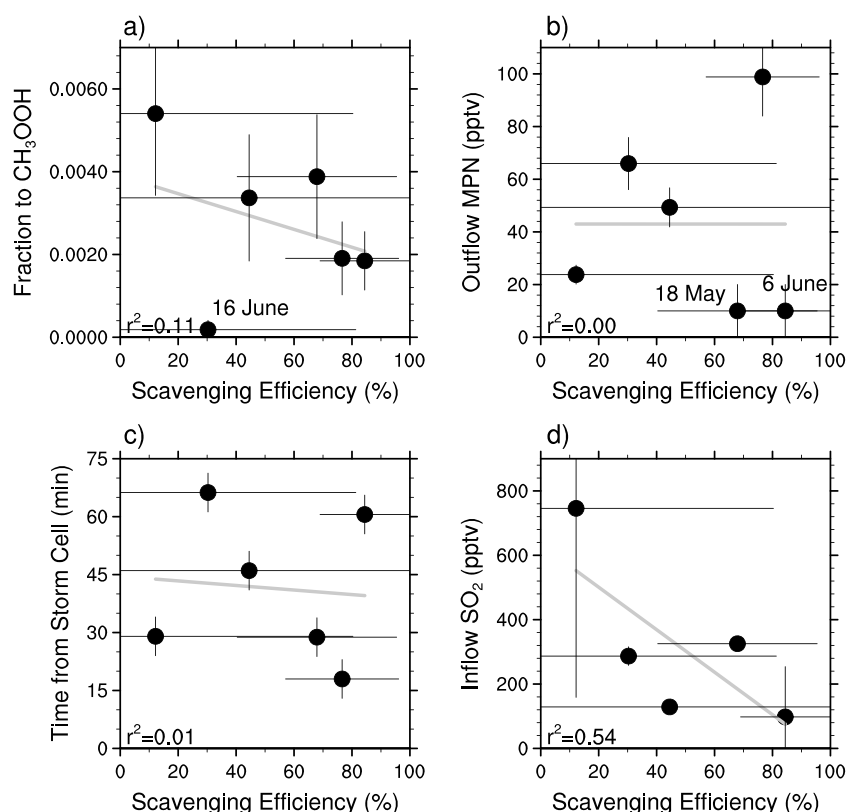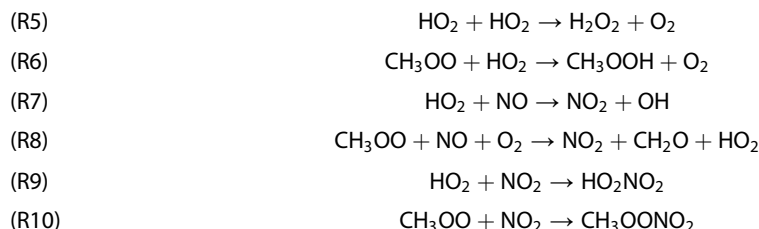
Figure 6. Correspondence of CH_3OOH scavenging efficiency with estimated (a) fraction of CH_3OO producing CH_3OOH, (b) 60 s averaged methyl peroxy nitrate data in the outflow flight leg, (c) time traveled by sampled air from storm cell to the aircraft in the outflow region, and (d) average SO_2 mixing ratio in the inflow region of the storm. See text for details on how each parameter was estimated. The gray line in each plot represents the regression line for the data shown.

The production of H_2O_2 is primarily from the hydroperoxy radical self-reaction (R5). Similarly, CH_3OOH is produced from methylperoxy radical reaction with the hydroperoxy radical (R6). However, NO and NO_2 reaction with peroxy radicals ((R7)–(R10)) compete with the peroxide production, causing less peroxide production at higher NO concentrations.

(R5) $$HO_2 + HO_2 \rightarrow H_2O_2 + O_2$$

(R6) $$CH_3OO + HO_2 \rightarrow CH_3OOH + O_2$$

(R7) $$HO_2 + NO \rightarrow NO_2 + OH$$

(R8) $$CH_3OO + NO + O_2 \rightarrow NO_2 + CH_2O + HO_2$$

(R9) $$HO_2 + NO_2 \rightarrow HO_2NO_2$$

(R10) $$CH_3OO + NO_2 \rightarrow CH_3OONO_2$$

In a thunderstorm, low NO conditions may exist in the inflow region of the storm, but as the air parcel rises generation of NO from lightning would create high NO conditions. While the peroxy radicals have other destruction reactions (e.g., $HO_2 + OH$ and reaction with other organic peroxy radicals), their contribution to peroxy radical loss is much smaller than the reactions listed in (R7)–(R10). Comparing the loss of CH_3OO via reaction with HO_2 (R6) with those via reactions with NO (R8) and NO_2 (R10) can illuminate whether the NO conditions are affecting the estimate of the CH_3OOH scavenging efficiency. We can define the fraction of CH_3OO to produce CH_3OOH (F_{Prod_CH3OOH}) as

$$F_{Prod\_CH3OOH} = \frac{k_6[HO_2]}{k_6[HO_2] + k_8[NO] + k_{10}[NO_2]} \quad (4)$$
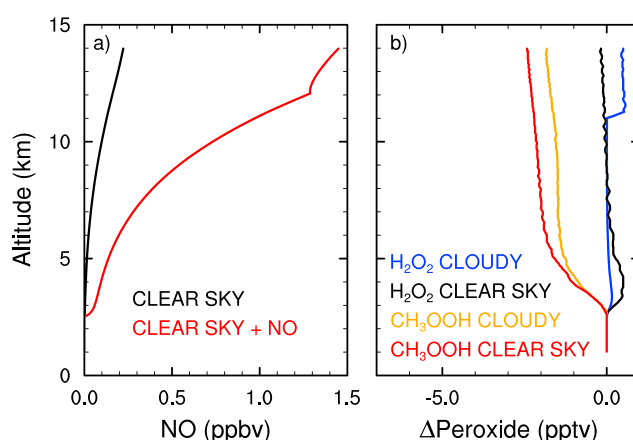
Figure 7. Vertical profiles of (a) gas-phase NO calculated by the photochemical gas-aqueous chemistry box model and (b) the difference between gas-phase H_2O_2 and CH_3OOH mixing ratios between the simulations with and without the NO source. The black and blue lines are H_2O_2 differences from the gas-only chemistry and gas-aqueous chemistry simulations, respectively. The red and orange lines are CH_3OOH differences from the gas-only and gas-aqueous chemistry simulations, respectively.

This fraction can be estimated using the DC-8 aircraft data for NO, NO_2, HO_2, and temperature. The calculated F_{Prod_CH3OOH} values are found to be <1% because of the high NO_x mixing ratios, which ranged from 0.7 to 2.5 ppbv, and low HO_2 mixing ratios (0.3–3.9 pptv) measured in the outflow flight legs. Comparing F_{Prod_CH3OOH} to the CH_3OOH scavenging efficiency (Figure 6a) shows a weak correlation between these two parameters, although five of the six storms analyzed have a strong correspondence with more CH_3OOH scavenged when its fraction produced is lower. Thus, it is uncertain whether increased NO_x from lightning production has an important effect on CH_3OOH gas-phase production.

Reaction (R10) produces methyl peroxy nitrate (MPN), which was measured by the TD-LIF instrument on the DC-8. A comparison of average MPN data in the outflow region with the CH_3OOH scavenging efficiencies shows no correspondence between the two parameters when all the storms are included in the comparison, but a strong correspondence between the two parameters if the data from 18 May and 6 June Colorado storms are not included in the calculation (Figure 6b). Despite the lack of correlation between MPN in the outflow region and the CH_3OOH scavenging efficiency shown here, the stronger correlation for four of the storms shows a potential correspondence between these two parameters. Thus, we encourage using MPN-CH_3OOH analysis in future efforts to understand CH_3OOH scavenging in thunderstorms.

To learn whether NO production from lightning could be a potential reason for CH_3OOH depletion in thunderstorm anvils, the gas-aqueous photochemical box model was used. The model began with the same conditions as described in section 2.4 but had a NO emission included representing lightning-NO_x production. The NO source was set to 10 pptv per time step (10 s) from the altitude where $T = 285$ K to the altitude where $T = 223$ K. This profile is based on the WRF-Chem results of NO mixing ratio in the updraft region. In Figure 7a, the NO vertical profiles from the simulations with and without the "lightning-NO_x" source are shown. The source of NO causes an increase of NO mixing ratios from ~0.1 ppbv to ~1.2 ppbv. Even with the increase in NO mixing ratios, both gas-phase H_2O_2 and CH_3OOH mixing ratios are unchanged from the simulations without the lightning-NO_x source (Figure 7b), although the change in CH_3OOH mixing ratios does show a <5 pptv decrease. Despite the null result from the parcel model calculations, the correlations shown above suggest that the chemistry with lightning-produced NO need to be further investigated with cloud-resolving chemistry models because of their ability to represent realistically the cloud dynamics and physics compared to a simple parcel model.

The results from the observational analyses do not depend on the time since the air parcel exited the storm core and was sampled by the DC-8 aircraft (Figure 6c), which was determined from the distance downwind of the storm core using Figure 2, divided by the horizontal wind speed measured aboard the aircraft. Indeed, the storms with the highest CH_3OOH scavenging efficiencies, 6 June and 29 May, have very different estimated times since the air parcel exited the storm core of ~60 min and ~18 min, respectively.

Aqueous-phase chemistry can also affect CH_3OOH mixing ratios in a storm via in-cloud reaction between CH_3OOH and HSO_3^- [*Seinfeld and Pandis*, 1998],

(A1) $$CH_3OOH + HSO_3^- + H^+ \rightarrow SO_4^{2-} + 2H^+ + CH_3OH$$
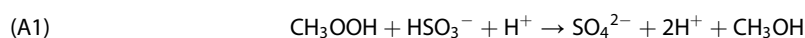
The hydroxyl radical OH can also oxidize CH_3OOH in the aqueous phase forming either CH_3OO radicals or CH_2O.

(A2) $$CH_3OOH + OH \rightarrow CH_3OO + H_2O$$

(A3) $$CH_3OOH + OH \rightarrow CH_3(OH)_2 + HO_2$$

Barth et al. [2007a] included reactions (A2) and (A3) in their cloud chemistry modeling of thunderstorm chemistry and found essentially the same scavenging efficiency when aqueous chemistry was included in the simulation as when aqueous chemistry was excluded. However, *Barth et al.* [2007a] did not include reaction (A1). To learn whether reaction (A1) may be important, the CH_3OOH scavenging efficiency is compared to the SO_2 inflow mixing ratios for each storm case. Unfortunately DC-8 SO_2 mixing ratios are not available for the 29 May storm, and the GV SO_2 measurements are likely not representative of inflow air because the GV low level sampling (2–3.5 km altitude) occurred just before storm initiation to the west of the DC-8 inflow legs. A comparison of the CH_3OOH scavenging efficiencies with inflow SO_2 for the other five storm cases shows a moderate anticorrelation, with more scavenging at low SO_2 conditions (Figure 6d). Intuitively, this anticorrelation seems to be the opposite of what is expected if aqueous-phase chemistry is reducing CH_3OOH. With a moderate anticorrelation between CH_3OOH scavenging efficiencies and inflow SO_2, it is not obvious if SO_2 is affecting CH_3OOH mixing ratios in the storm outflow region. In contrast, H_2O_2 scavenging efficiencies do have a positive correspondence with the inflow SO_2 mixing ratio (not shown) but do not have a strong correlation because of the nearly complete removal of H_2O_2 in two cases. This is a result of H_2O_2 mixing ratios in the outflow region being near the uncertainty offset of the H_2O_2 measurement for the storms with scavenging efficiencies $\geq 89\%$.

5. Conclusion

We have analyzed DC3 observations of hydrogen peroxide and methyl hydrogen peroxide to determine their scavenging efficiencies in thunderstorms observed in the High Plains of northeast Colorado and Southern Great Plains of Oklahoma. The analysis method, which is similar to that described by A. Fried et al. (submitted manuscript, 2016), first finds an entrainment rate for each storm by using mixing ratios of *n*-butane, *i*-butane, *n*-pentane, and *i*-pentane, which are all sufficiently chemically long-lived and insoluble to be good tracers of transport, in the inflow and outflow regions, and clear-air vertical profiles. Once the entrainment rate is determined, the peroxide scavenging efficiencies are found from the measurements from the same inflow, outflow, and clear-sky regions. The calculated H_2O_2 and CH_3OOH scavenging efficiencies are 79–97% and 12–84%, respectively, for six DC3 storms analyzed. The scavenging efficiency relative uncertainties (= uncertainty/average) are high, 5–25% and 18–558% for H_2O_2 and CH_3OOH, respectively, and are mostly from the uncertainties of the peroxide measurements. The cloud resolving modeling by *Bela et al.* [2016] predicts scavenging efficiencies similar to those observed for the 29 May 2012 DC3 storm when the retention efficiency of H_2O_2 and CH_3OOH dissolved in freezing drops was 25% or greater for H_2O_2 and 100% for CH_3OOH. These modeling results suggest that the degree of riming of cloud drops by snow and graupel could affect the amount of CH_3OOH scavenged by the storms.

We investigated several environmental, storm morphological, and chemical parameters that may contribute to the wide range of calculated CH_3OOH scavenging efficiencies. While the thermodynamic environment (e.g., CAPE and 0–6 km vertical wind shear) plays a role in the degree of scavenging, it does not explain why CH_3OOH scavenging has such a large range for the six storms examined, although the volume of the 35 dBZ region is slightly correlated with CH_3OOH scavenging efficiencies. The 35 dBZ region is often representative of regions where graupel and hail reside, suggesting cloud physical processes, e.g., riming, may be affecting the CH_3OOH scavenging efficiencies. We found that more CH_3OOH was scavenged at low entrainment rates and less CH_3OOH was scavenged at high entrainment rates in storms. This correlation may be connected with the shape of the CH_3OOH vertical profile in clear sky since the peroxide profiles usually did not decrease sharply with altitude like the butane and pentane vertical profiles, from which the entrainment rate was derived. Further, the variability of entrainment rate with height (as prescribed by the cloud resolving model simulation) does not significantly change the calculated scavenging efficiencies.

The production of NO from lightning may influence CH_3OOH mixing ratios in the convective outflow by increasing the $CH_3OO + NO$ and the $CH_3OO + NO_2$ reaction rates, which reduces the production of CH_3OOH via $CH_3OO + HO_2$. Correlations between the CH_3OOH scavenging efficiency and the fraction of CH_3OO producing CH_3OOH and between the scavenging efficiency and methyl peroxy nitrate suggest such a connection for a few of the storm cases analyzed. We recommend future analyses of peroxide scavenging considering this possible reduced chemical production rate as a contribution to low CH_3OOH mixing ratios in convective outflows, although our gas-aqueous photochemical box model shows that gas-phase CH_3OOH mixing ratios are unchanged when a NO source is included in the simulation. CH_3OOH can also be destroyed in the aqueous phase via reaction with bisulfite ion (the dominant form of SO_2 in cloud droplets), suggesting a positive correlation between CH_3OOH scavenging efficiencies and the inflow SO_2 mixing ratios. However, we found a moderate anticorrelation between these two quantities indicating that the aqueous-phase chemistry may not contribute to the wide range of scavenging efficiencies found.

The analysis done here, via correlations between measured variables and calculated scavenging efficiency and process-scale modeling, suggests that dynamical, physical, and chemical processes affect CH_3OOH in the outflow of thunderstorms. The amount of hail in the storm plays an important role in two ways. First, the production of hail involves substantial riming of cloud droplets by falling snow and graupel, especially as the graupel and hail are recirculated in the storms. A portion of a trace gas dissolved in the cloud droplets would be retained in the precipitating hail and subsequently removed from the atmosphere. Hail also plays a key role in triggering lightning. The NO produced from lightning reduces the production of gas-phase CH_3OOH because of NO and NO_2 reactions with CH_3OO (a key precursor of CH_3OOH) forming formaldehyde, NO_2, and methyl peroxy nitrate. However, photochemical box model simulations do not confirm that increased NO causes decreased CH_3OOH mixing ratios at the top of the storm core. This investigation provides guidance for future studies on understanding the complex interactions between storms and chemistry for peroxides. To more thoroughly understand these interactions, cloud chemistry modeling that explores the various effects of entrainment, hail (especially its role in scavenging soluble trace gases via the riming of cloud droplets), lightning-NO_x, and other chemistry precursors should be pursued.

Previous studies estimated CH_3OOH scavenging efficiencies to be $<10\%$; thus, the high scavenging efficiencies found in this study are surprising and could have implications on the chemistry downwind of convection in the upper troposphere. The low CH_3OOH mixing ratios (100–350 pptv) in the convective outflow observed here would produce, via CH_3OOH photolysis and OH oxidation, less CH_2O and HO_x radicals than if less CH_3OOH were scavenged. Thus, the high scavenging efficiencies of CH_3OOH may explain discrepancies between photochemical box model calculations and measurements of CH_2O in convective outflow plumes, similar to those described by *Fried et al.* [2003]. It is expected that the low H_2O_2 and CH_3OOH mixing ratios in the convective outflow would have a smaller contribution to downwind O_3 production compared to CH_2O, whose mixing ratios in the convective outflow ranged from 600 to 1500 pptv (A. Fried et al., submitted manuscript, 2016). The contribution of CH_2O and the peroxides to UT O_3 formation can be pursued further via model calculations.

References

Barth, M. C., D. A. Hegg, P. V. Hobbs, J. G. Walega, G. L. Kok, B. G. Heikes, and A. L. Lazrus (1989), Measurements of atmospheric gas-phase and aqueous-phase hydrogen peroxide concentrations in winter on the east coast of the United States, *Tellus B*, *41*, 61–69.

Barth, M. C., A. L. Stuart, and W. C. Skamarock (2001), Numerical simulations of the July 10, 1996 Stratospheric-Tropospheric Experiment: Radiation, Aerosols, and Ozone/deep convection experiment storm: Redistribution of soluble tracers, *J. Geophys. Res.*, *106*, 12,381–12,400, doi:10.1029/2001JD900139.

Barth, M. C., P. G. Hess, and S. Madronich (2002), Effect of marine boundary layer clouds on tropospheric chemistry as analyzed in a regional chemistry transport model, *J. Geophys. Res.*, *107*(D11), 4126, doi:10.1029/2001JD000468.

Barth, M. C., S. Sillman, R. Hudman, M. Z. Jacobson, C.-H. Kim, A. Monod, and J. Liang (2003), Summary of the cloud chemistry modeling intercomparison: Photochemical box model simulation, *J. Geophys. Res.*, *108*(D7), 4214, doi:10.1029/2002JD002673.

Barth, M. C., S.-W. Kim, W. C. Skamarock, A. L. Stuart, K. E. Pickering, and L. E. Ott (2007a), Simulations of the redistribution of formaldehyde, formic acid, and peroxides in the 10 July 1996 Stratospheric-Tropospheric Experiment: Radiation, Aerosols, and Ozone deep convection storm, *J. Geophys. Res.*, *112*, D13310, doi:10.1029/2006JD008046.

Barth, M. C., et al. (2007b), Cloud-scale model intercomparison of chemical constituent transport in deep convection, *Atmos. Chem. Phys.*, *7*, 4709–4731, doi:10.5194/acp-7-4709-2007.

Barth, M. C., et al. (2015), The Deep Convective Clouds and Chemistry (DC3) field campaign, *Bull. Am. Meteor. Soc.*, *96*, 1281–1309, doi:10.1175/BAMS-D-13-00290.1.

Bela, M. M., et al. (2016), Wet scavenging of soluble gases in DC3 deep convective storms using WRF-Chem simulations and aircraft observations, *J. Geophys. Res. Atmos.*, *121*, doi:10.1002/2015JD024623.

Borbon, A., et al. (2012), Transport and chemistry of formaldehyde by mesoscale convective systems in West Africa during AMMA 2006, *J. Geophys. Res.*, *117*, D12301, doi:10.1029/2011JD017121.

Brasseur, A.-L., R. Ramaroson, A. Delannoy, W. Skamarock, and M. Barth (2002), Three-dimensional calculation of photolysis frequencies in the presence of clouds, *J. Atmos. Chem.*, *41*, 211–237.

Browne, E. C., et al. (2011), Global and regional effects of the photochemistry of CH3O2NO2: evidence from ARCTAS, *Atmos. Chem. Phys.*, *11*, 4209–4219, doi:10.5194/acp-11-4209-2011.

Chang, J. S., R. A. Brost, I. S. A. Isaksen, S. Madronich, P. Middleton, W. R. Stockwell, and C. J. Walcek (1987), A three-dimensional Eulerian acid deposition model: Physical concepts and formulation, *J. Geophys. Res.*, *92*(D12), 14,681–14,700, doi:10.1029/JD092iD12p14681.

Chin, M., P. Ginoux, S. Kinne, O. Torres, B. N. Holben, B. N. Duncan, R. V. Martin, J. A. Logan, A. Higurashi, and T. Nakajima (2002), Tropospheric aerosol optical thickness from the gocart model and comparisons with satellite and sun photometer measurements, *J. Atmos. Sci.*, *59*(3), 461–483, doi:10.1175/1520-0469(2002)059h0461:TAOTFTi2.0.CO;2.

Cohan, D. S., M. G. Schultz, D. J. Jacob, B. G. Heikes, and D. R. Blake (1999), Convective injection and photochemical decay of peroxides in the tropical upper troposphere: Methyl iodide as a tracer of marine convection, *J. Geophys. Res.*, *104*, 5717–5724, doi:10.1029/98JD01963.

Colman, J. J., A. L. Swanson, S. Meinardi, B. C. Sive, D. R. Blake, and F. S. Rowland (2001), Description of the analysis of a wide range of volatile organic compounds in whole air samples collected during PEM-Tropics A and B, *Anal. Chem.*, *73*, 3723–3731.

Cotton, W. R., G. D. Alexander, R. Hertenstein, R. L. Walko, R. L. McAnelly, and M. Nicholls (1995), Cloud venting—A review and some new global annual estimates, *Earth Sci. Rev.*, *38*, 169–206.

Crounse, J. D., K. A. McKinney, A. J. Kwan, and P. O. Wennberg (2006), Measurement of gas-phase hydroperoxides by chemical ionization mass spectrometry, *Anal. Chem.*, *2006*(78), 6726–6732, doi:10.1021/ac0604235.

Crum, T. D., and R. L. Alberty (1993), The WSR-88D operational support facility, *Bull. Am. Meteorol. Soc.*, *74*(9), 1669–1687.

Crutzen, P. J., and M. G. Lawrence (2000), The impact of precipitation scavenging on the transport of trace gases: A 3-dimensional model sensitivity study, *J. Atmos. Chem.*, *37*, 81–112.

Emmons, L. K., et al. (2010), Description and evaluation of the model for ozone and related chemical tracers, version 4 (MOZART-4), *Geosci. Model Dev.*, *3*(1), 43–67, doi:10.5194/gmd-3-43-2010.

Faloona, I. C., et al. (2004), A laser-induced fluorescence instrument for detecting tropospheric OH and HO_2: Characteristics and calibration, *J. Atmos. Chem.*, *47*, 139–167, doi:10.1023/B:JOCH.0000021036.53185.0e.

Fierro, A. O., E. R. Mansell, C. L. Ziegler, and D. R. MacGorman (2012), Application of a lightning data assimilation technique in the wrf-arw model at cloud-resolving scales for the tornado outbreak of 24 may 2011, *Mon. Weather Rev.*, *140*(8), 2609–2627, doi:10.1175/MWR-D-11-00299.1.

Fried, A., et al. (2003), Airborne tunable diode laser measurements of formaldehyde during TRACE-P: Distributions and box model comparisons, *J. Geophys. Res.*, *108*(D20), 8798, doi:10.1029/2003JD003451.

Gilman, J. B., B. M. Lerner, W. C. Kuster, and J. A. de Gouw (2013), Source signature of volatile organic compounds from oil and natural gas operations in Northeastern Colorado, *Environ. Sci. Technol.*, *47*, 1297–1305.

Grell, G. A., S. E. Peckham, R. Schmitz, S. A. McKeen, G. Frost, W. C. Skamarock, and B. Eder (2005), Fully coupled "online" chemistry in the WRF model, *Atmos. Environ.*, *39*, 6957–6976.

Guenther, A., T. Karl, P. Harley, C. Wiedinmyer, P. I. Palmer, and C. Geron (2006), Estimates of global terrestrial isoprene emissions using MEGAN (Model of Emissions of Gases and Aerosols from Nature), *Atmos. Chem. Phys.*, *6*(11), 3181–3210, doi:10.5194/acp-6-3181-2006.

Homeyer, C. R. (2014), Formation of the enhanced-v infrared cloud-top feature from high-resolution three-dimensional radar observations, *J. Atmos. Sci.*, *71*, 332–348, doi:10.1175/JAS-D-13-079.1.

Homeyer, C. R., and M. R. Kumjian (2015), Microphysical characteristics of overshooting convection from polarimetric radar observations, *J. Atmos. Sci.*, *72*, 870–891, doi:10.1175/JAS-D-13-0388.1.

Hong, S.-Y., Y. Noh, and J. Dudhia (2006), A new vertical diffusion package with an explicit treatment of entrainment processes, *Mon. Weather Rev.*, *134*(9), 2318–2341, doi:10.1175/MWR3199.1.

Hudman, R. C., et al. (2007), Surface and lightning sources of nitrogen oxides over the United States: Magnitudes, chemical evolution, and outflow, *J. Geophys. Res.*, *112*, D12S05, doi:10.1029/2006JD007912.

Huntrieser, H., et al. (2016a), On the origin of pronounced O3 gradients in the thunderstorm outflow region during DC3, *J. Geophys. Res. Atmos.*, *121*, doi:10.1002/2015JD024279.

Huntrieser, H., et al. (2016b), Injection of lightning-produced NOx, water vapor, wildfire emissions, and stratospheric air to the UT/LS as observed from DC3 measurements, *J. Geophys. Res. Atmos.*, *121*, doi:10.1002/2015JD024273.

Iacono, M. J., J. S. Delamere, E. J. Mlawer, M. W. Shephard, S. A. Clough, and W. D. Collins (2008), Radiative forcing by long-lived greenhouse gases: Calculations with the AER radiative transfer models, *J. Geophys. Res.*, *113*, D13103, doi:10.1029/2008JD009944.

Jaeglé, L., et al. (1997), Observed OH and HO_2 in the upper troposphere suggest a major source from convective injection of peroxides, *Geophys. Res. Lett.*, *24*, 3181–3184, doi:10.1029/97GL03004.

Kim, S., et al. (2007), Measurement of HO2NO2 in the free troposphere during the Intercontinental Chemical Transport Experiment–North America 2004, *J. Geophys. Res.*, *112*, D12S01, doi:10.1029/2006JD007676.

Kim, S.-W., M. C. Barth, and M. Trainer (2012), Influence of fair-weather clouds on isoprene chemistry, *J. Geophys. Res.*, *117*, D10302, doi:10.1029/2011JD017099.

Lawson, R. P., D. O'Connor, P. Zmarzly, K. Weaver, B. Baker, and Q. Mo (2006), The 2D-S (Stereo) probe: Design and preliminary tests of a new airborne, high-speed, high-resolution particle imaging probe, *J. Atmos. Oceanic Technol.*, *23*, 1462–1477.

Lee, S. S., L. J. Donner, V. T. J. Phillips, and Y. Ming (2008), The dependence of aerosol effects on clouds and precipitation on cloud-system organization, shear and stability, *J. Geophys. Res.*, *113*, D16202, doi:10.1029/2007JD009224.

Leriche, M., J.-P. Pinty, C. Mari, and D. Gazen (2013), A cloud chemistry module for the 3-D cloud-resolving mesoscale model Meso-NH with application to idealized cases, *Geosci. Model Dev.*, *6*, 1275–1298, doi:10.5194/gmd-6-1275-2013.

Luo, Z. J., G. Y. Liu, and G. L. Stephens (2010), Use of A-Train data to estimate convective buoyancy and entrainment rate, *Geophys. Res. Lett.*, *37*, L09804, doi:10.1029/2010GL042904.

Macdonald, A. M., K. G. Anlauf, C. M. Banic, W. R. Leaitch, and H. A. Wiebe (1995), Airborne measurements of aqueous and gaseous hydrogen peroxide during spring and summer in Ontario, Canada, *J. Geophys. Res.*, *100*(D4), 7253–7262, doi:10.1029/95JD00194.

Morrison, H., G. Thompson, and V. Tatarskii (2009), Impact of cloud microphysics on the development of trailing stratiform precipitation in a simulated squall line: Comparison of one- and two-moment schemes, *Mon. Weather Rev.*, *137*(3), 991–1007, doi:10.1175/2008MWR2556.1.

Nault, B. A., C. Garland, S. E. Pusede, P. J. Wooldridge, K. Ullmann, S. R. Hall, and R. C. Cohen (2015), Measurements of $CH_3O_2NO_2$ in the upper troposphere, *Atmos. Meas. Tech.*, *8*, 987–997, doi:10.5194/amt-8-987-2015.

Neu, J. L., and M. J. Prather (2012), Toward a more physical representation of precipitation scavenging in global chemistry models: Cloud overlap and ice physics and their impact on tropospheric ozone, *Atmos. Chem. Phys.*, *12*, 3289–3310, doi:10.5194/acp-12-3289-2012.

Nguyen, T. B., J. D. Crounse, A. P. Teng, J. M. St. Clair, F. Paulot, G. M. Wolfe, and P. O. Wennberg (2015), Rapid deposition of oxidized biogenic compounds to a temperate forest, *Proc. Natl. Acad. Sci. U.S.A.*, *112*, E392–E401, doi:10.1073/pnas.1418702112.

Paulot, F., J. D. Crounse, H. G. Kjaergaard, A. Kurten, J. M. S. Clair, J. H. Seinfeld, and P. O. Wennberg (2009), Unexpected epoxide formation in the gas-phase photooxidation of isoprene, *Science*, *325*(5941), 730–733.

Pollack, I. B., B. M. Lerner, and T. B. Ryerson (2011), Evaluation of ultraviolet light-emitting diodes for detection of atmospheric NO_2 by photolysis—Chemiluminescence, *J. Atmos. Chem.*, *65*(2), 111–125, doi:10.1007/s10874-011-9184-3.

Prather, M. J., and D. J. Jacob (1997), A persistent imbalance in HOx and NOx photochemistry of the upper troposphere driven by deep tropical convection, *Geophys Res. Lett.*, *24*, 3189–3192, doi:10.1029/97GL03027.

Ravetta, F., et al. (2001), Experimental evidence for the importance of convected methylhydroperoxide as a source of hydrogen oxide (HOx) radicals in the tropical upper troposphere, *J. Geophys. Res.*, *106*, 32,709–32,716, doi:10.1029/2001JD900009.

Sachse, G. W., J. E. Collins, G. F. Hill, L. O. Wade, L. G. Burney, and J. A. Ritter (1991), Airborne tunable diode laser sensor for high-precision concentration and flux measurements of carbon monoxide and methane, *Proc. SPIE*, *1433*, 157–166, doi:10.1117/12.46162.

Sander, R. (2015), Compilation of Henry's law constants (version 4.0) for water as solvent, *Atmos. Chem. Phys.*, *15*, 4399–4981, doi:10.5194/acp-15-4399-2015.

Sander, S. P., et al. (2011), Chemical Kinetics and Photochemical Data for Use in Atmospheric Studies, Evaluation No. 17, JPL Publication 10–6, Jet Propulsion Laboratory, Pasadena, http://jpldataeval.jpl.nasa.gov.

Scala, J. R., et al. (1990), Cloud draft structure and trace gas transport, *J. Geophys. Res.*, *95*(D10), 17,015–17,030, doi:10.1029/JD095iD10p17015.

Schroeder, J. R., L. L. Pan, T. Ryerson, G. Diskin, J. Hair, S. Meinardi, I. Simpson, B. Barletta, N. Blake, and D. R. Blake (2014), Evidence of mixing between polluted convective outflow and stratospheric air in the upper troposphere during DC3, *J. Geophys. Res. Atmos.*, *119*, 11,477–11,491, doi:10.1002/2014JD022109.

Seinfeld, J., and S. Pandis (1998), *Atmospheric Chemistry and Physics: From Air Pollution to Climate Change*, Wiley, New York.

Simpson, I. J., et al. (2010), Characterization of trace gases measured over Alberta oil sands mining operations: 76 speciated C2–C10 volatile organic compounds (VOCs), CO2, CH4, CO, NO, NO2, NOy, O3 and SO2, *Atmos. Chem. Phys.*, *10*, 11,931–11,954, doi:10.5194/acp-10-11931-2010.

Skamarock, W. C., J. G. Powers, M. Barth, J. E. Dye, T. Matejka, D. Bartels, K. Baumann, J. Stith, D. D. Parrish, and G. Hubler (2000), Numerical simulations of the July 10 Stratospheric-Tropospheric Experiment: Radiation, Aerosols, and Ozone/Deep Convection Experiment convective system: Kinematics and transport, *J. Geophys. Res.*, *105*(D15), 19,973–19,990, doi:10.1029/2000JD900179.

Snow, J. A., B. G. Heikes, H. Shen, D. W. O'Sullivan, A. Fried, and J. Walega (2007), Hydrogen peroxide, methyl hydroperoxide, and formaldehyde over North America and the North Atlantic, *J. Geophys. Res.*, *112*, D12S07, doi:10.1029/2006JD007746.

St. Clair, J. M., D. C. McCabe, J. D. Crounse, U. Steiner, and P. O. Wennberg (2010), Chemical ionization tandem mass spectrometer for the in situ measurement of methyl hydrogen peroxide, *Rev. Sci. Instrum.*, *81*(9), 094102, doi:10.1063/1.3480552.

Stuart, A. L., and M. Z. Jacobson (2006), A numerical model of the partitioning of trace chemical solutes during drop freezing, *J. Atmos. Chem.*, *53*, 13–42.

Swarthout, R. F., R. S. Russo, Y. Zhou, A. H. Hart, and B. C. Sive (2013), Volatile organic compound distributions during the NACHTT campaign at the Boulder Atmospheric Observatory: Influence of urban and natural gas sources, *J. Geophys. Res. Atmos.*, *118*, 10,614–10,637.

Taylor, J. R. (1982), *An Introduction to Error Analysis: The Study of Uncertainties in Physical Measurements*, University Science Books, Mill Valley, Calif.

Thompson, A. M., K. E. Pickering, R. R. Dickerson, W. G. Ellis Jr., D. J. Jacob, J. R. Scala, W.-K. Tao, D. P. McNamara, and J. Simpson (1994), Convective transport over the central United States and its role in regional CO and ozone budgets, *J. Geophys. Res.*, *99*(D9), 18,703–18,711, doi:10.1029/94JD01244.

Thornton, J. A., P. J. Wooldridge, and R. C. Cohen (2000), Atmospheric NO_2: In situ laser-induced fluorescence detection at parts per trillion mixing ratios, *Anal. Chem.*, *72*, 528–539.

Wang, C. (2005), A modeling study of the response of tropical deep convection to the increase of cloud condensation nuclei concentration: 2. Radiation and tropospheric chemistry, *J. Geophys. Res.*, *110*, D22204, doi:10.1029/2005JD005829.

Weisman, M. L., and J. B. Klemp (1982), The dependence of numerically simulated convective storms on vertical wind shear and buoyancy, *Mon. Weather Rev.*, *110*, 504–520, doi:10.1175/1520-0493(1982)110<0504:TDONSC>2.0.CO;2.

Weisman, M. L., J. B. Klemp, and R. Rotunno (1988), Structure and evolution of numerically simulated squall lines, *J. Atmos. Sci.*, *45*, 1990–2013, doi:10.1175/1520-0469(1988)045<1990:SAEONS>2.0.CO;2.

Wennberg, P. O., et al. (1998), Hydrogen radicals, nitrogen radicals, and the production of O_3 in the upper troposphere, *Science*, *279*, 49–53.

Wesely, M. (1989), Parameterization of surface resistances to gaseous dry deposition in regional-scale numerical models, *Atmos. Environ.*, *23*, 1293–1304.

Wiedinmyer, C., S. K. Akagi, R. J. Yokelson, L. K. Emmons, J. A. Al-Saadi, J. J. Orlando, and A. J. Soja (2011), The fire inventory from NCAR (FINN): A high resolution global model to estimate the emissions from open burning, *Geosci. Model Dev.*, *4*(3), 625–641, doi:10.5194/gmd-4-625-2011.

Yang, Q., et al. (2015), Aerosol transport and wet scavenging in deep convective clouds: A case study and model evaluation using a multiple passive tracer analysis approach, *J. Geophys. Res. Atmos.*, *120*, 8448–8468, doi:10.1002/2015JD023647.